PTEP

Prog. Theor. Exp. Phys. **2022** 063B05(33 pages)
DOI: 10.1093/ptep/ptac068

Possibility of a multi-step electroweak phase transition in the two-Higgs doublet models

Mayumi Aoki, Takatoshi Komatsu, and Hiroto Shibuya*

Institute for Theoretical Physics, Kanazawa University, Kanazawa 920-1192, Japan
*E-mail: h_shibuya@hep.s.kanazawa-u.ac.jp

Received January 9, 2022; Revised March 29, 2022; Accepted April 18, 2022; Published May 19, 2022

We discuss whether a multi-step electroweak phase transition (EWPT) occurs in two-Higgs doublet models (2HDMs). The EWPT is related to interesting phenomena such as baryogenesis and the ensuing gravitational wave. We examine parameter regions in CP-conserving 2HDMs and find certain areas where multi-step EWPTs occur. The parameter search shows the multi-step EWPT prefers the scalar potential with the approximate Z_2 symmetry and a mass hierarchy between the neutral CP-odd and CP-even extra scalar bosons $m_A < m_H$. By contrast, the multi-step EWPT whose first step is strongly first order favors a mass hierarchy $m_A > m_H$. In addition, we compute the Higgs trilinear coupling in the parameter region where multi-step EWPTs occur, which can be observed at future colliders. We also discuss a multi-peaked gravitational wave from a multi-step EWPT. Subject index B53, B59

1. Introduction

Although the standard model (SM) of particle physics has been verified through various experiments, the asymmetry of the baryon number in the universe is still one of the big problems. The observable of baryon to radiation number ratio is $\eta_B \equiv n_B/n_\gamma = (6.12 \pm 0.04) \times 10^{-10}$ [1]. To explain this asymmetry, the theory must satisfy Sakharov's three conditions [2]. The conditions are violation of baryon numbers, violation of C and CP symmetries, and departure from thermal equilibrium. To generate baryon asymmetry at the electroweak (EW) scale via EW baryogenesis (EWBG) [3], the EW phase transition (EWPT) needs to be strongly first order. However, lattice simulations show that the mass of the Higgs boson must be less than about 70 GeV to make the EWPT first order in the SM [4,5], and the observed Higgs boson with a mass of 125 GeV [6–9] indicates that the EWPT in the SM is crossover [10]. Furthermore, sufficient baryon asymmetry cannot be produced via the Cabibbo–Kobayashi–Maskawa phase, so that EWBG cannot be achieved successfully in the SM [11–13]. Sufficient baryon asymmetry can be generated via the EWBG scenario by extending the scalar sector of the SM. One of the simplest extensions is the two-Higgs doublet model (2HDM), where an $SU(2)$ scalar doublet is added to the SM.[1] Since the 2HDM has new CP-violating sources in the scalar potential, it has the possibility of achieving EWBG. However, the model has difficulty producing suffi-

[1] For studies of the strong one-step phase transitions (PTs) in CP-conserving 2HDMs, see, e.g., Refs. [14–18]. For non-perturbative analyses, see Refs. [19,20].

Funded by SCOAP[3]

cient baryon number because the electric dipole moment (EDM) measurements constrain the sources strictly [21–23].[2]

One could come up with the idea of solving the above difficulty in 2HDMs by considering a multi-step EWPT [25]. A sufficient baryon number is produced at the first PT step if it is strongly first order and enough CP violation exists, while the baryon number cannot be washed out at subsequent PT(s) if the EW sphaleron processes are sufficiently suppressed. Consequently, a sufficient baryon number is preserved at the EW vacuum even if it is a CP-conserving vacuum. The reason why we consider baryon asymmetry produced at the first step is that the first-order PT at the subsequent step occurs between $SU(2)$ broken phases. Therefore, the sphaleron processes are suppressed in both phases and sufficient asymmetry would not be produced [26, 27].[3] Another interesting phenomenon derived from the multi-step PT is a multi-peaked gravitational wave (GW). Since a first-order PT yields a GW spectrum [28, 29], the superposed GW can have multiple peaks if the first-order PT occurs multiple times, which could be observed by future space-based interferometers such as the approved Laser Interferometer Space Antenna (LISA) [30–32]. Previous research concerning multi-step PTs examined singlet extensions [33–47], inert 2HDMs [25, 26, 48–50], 2HDMs [16, 27, 51], triplet extensions [52–55], and other models [56–70].

In this paper we study multi-step EWPTs in CP-conserving 2HDMs. Because of the absence of a new CP-violating source, EWBG does not work and we will not discuss it. Studying the CP-violating case remains as future work. The main purpose of this paper is to reveal features of the multi-step PTs. By performing parameter searches, we find certain parameter spaces where multi-step PTs occur. Furthermore, to examine the possibility of verifying multi-step PT at collider experiments, we compute the deviation of the Higgs trilinear coupling from that in the SM. It is known that the deviation can be large in 2HDMs [71, 72] (see also Refs. [73, 74] for recent work), and it will be observed more precisely in future colliders like the High-Luminosity Large Hadron Collider (HL-LHC) [75] and International Linear Collider (ILC) [76]. We find that the deviation has a tendency to be large in certain regions when multi-step PTs occur. In addition, we calculate a two-peaked GW spectrum yielded by a two-step PT, which can be observed using LISA, the Big Bang Observer (BBO) [77], and the Ultimate Deci-Hertz Interferometer Gravitational Wave Observatory (U-DECIGO) [78].

The outline of this paper is as follows: In Sect. 2 we introduce the generic characteristics of 2HDMs. Section 3 is dedicated to giving the thermal effective potential. The theoretical constraints considered in our numerical analyses are briefly introduced in Sect. 4. In Sect. 5 we show the results of the parameter search for multi-step PT. Moreover, in Sect. 6 we discuss the predictions for the Higgs trilinear couplings as collider signatures, and for multi-peaked GWs as the cosmological signature for multi-step PTs. Our conclusions are given in Sect. 7.

[2] In the aligned 2HDM there is the possibility of evading the EDM constraints through cancellations among contributions to the EDMs even when CP-violating phases are unsuppressed [24].

[3] Reference [26] shows that sufficient baryon asymmetry is difficult to generate at the subsequent PT in the inert 2HDM. Also, Ref. [27] mentions that the second-step PT would not generate sufficient asymmetry in the 2HDMs.

2. The two-Higgs doublet model

The tree-level scalar potential of a CP-conserving 2HDM with a softly broken Z_2 symmetry is written as

$$V(\Phi_1, \Phi_2) = m_1^2 \Phi_1^\dagger \Phi_1 + m_2^2 \Phi_2^\dagger \Phi_2 - m_3^2 \left(\Phi_1^\dagger \Phi_2 + \Phi_2^\dagger \Phi_1\right) + \frac{\lambda_1}{2}\left(\Phi_1^\dagger \Phi_1\right)^2 + \frac{\lambda_2}{2}\left(\Phi_2^\dagger \Phi_2\right)^2 + \lambda_3 \left(\Phi_1^\dagger \Phi_1\right)\left(\Phi_2^\dagger \Phi_2\right) + \lambda_4 \left(\Phi_1^\dagger \Phi_2\right)\left(\Phi_2^\dagger \Phi_1\right) + \frac{\lambda_5}{2}\left[\left(\Phi_1^\dagger \Phi_2\right)^2 + \left(\Phi_2^\dagger \Phi_1\right)^2\right], \tag{1}$$

where Φ_i $(i = 1, 2)$ are the $SU(2)$ scalar doublets,

$$\Phi_i = \begin{pmatrix} w_i^+ \\ \frac{1}{\sqrt{2}}(v_i + h_i + i z_i) \end{pmatrix}. \tag{2}$$

We assume here that only the neutral CP-even scalar fields have vacuum expectation values (VEVs) v_i, which are real and positive, and satisfy $v \equiv \sqrt{v_1^2 + v_2^2} = 246\,\text{GeV}$. The third term with m_3^2 on the right-hand side in Eq. (1) breaks the Z_2 symmetry in the potential softly. The coefficients are taken to be real, although m_3^2 and λ_5 are complex parameters in general. Regarding only the neutral CP-even fields ϕ_i, the Φ_i become

$$\Phi_i = \begin{pmatrix} 0 \\ \frac{\phi_i}{\sqrt{2}} \end{pmatrix}. \tag{3}$$

Consequently, the tree-level scalar potential in Eq. (1) with the doublets in Eq. (3) is

$$V_0(\phi_1, \phi_2) = \frac{m_1^2}{2}\phi_1^2 + \frac{m_2^2}{2}\phi_2^2 - m_3^2 \phi_1 \phi_2 + \frac{\lambda_1}{8}\phi_1^4 + \frac{\lambda_2}{8}\phi_2^4 + \frac{1}{4}(\lambda_3 + \lambda_4 + \lambda_5)(\phi_1 \phi_2)^2. \tag{4}$$

The minimum value of $V_0(\phi_1, \phi_2)$ is given by $\phi_i = v_i$. From the minimum conditions, $\partial V_0/\partial \phi_i|_{\phi_i = v_i} = 0$, we obtain

$$m_1^2 = m_3^2 \tfrac{v_2}{v_1} - \tfrac{\lambda_1}{2} v_1^2 - \tfrac{1}{2}(\lambda_3 + \lambda_4 + \lambda_5) v_2^2, \tag{5}$$

$$m_2^2 = m_3^2 \tfrac{v_1}{v_2} - \tfrac{\lambda_2}{2} v_2^2 - \tfrac{1}{2}(\lambda_3 + \lambda_4 + \lambda_5) v_1^2. \tag{6}$$

To calculate the effective potential we introduce field-dependent masses because we need the masses of all fields at each of the coordinates (ϕ_1, ϕ_2) that contribute to the potential at the loop level. The field-dependent mass matrices of the charged and the neutral CP-odd scalar fields in the gauge basis are respectively given by

$$\mathcal{M}_{w^\pm}^2 = \frac{1}{2}\begin{pmatrix} 2m_1^2 + \lambda_1 \phi_1^2 + \lambda_3 \phi_2^2 & -2m_3^2 + (\lambda_4 + \lambda_5)\phi_1 \phi_2 \\ -2m_3^2 + (\lambda_4 + \lambda_5)\phi_1 \phi_2 & 2m_2^2 + \lambda_2 \phi_2^2 + \lambda_3 \phi_1^2 \end{pmatrix},$$

$$\mathcal{M}_z^2 = \frac{1}{2}\begin{pmatrix} 2m_1^2 + \lambda_1 \phi_1^2 + (\lambda_3 + \lambda_4 - \lambda_5)\phi_2^2 & -2m_3^2 + 2\lambda_5 \phi_1 \phi_2 \\ -2m_3^2 + 2\lambda_5 \phi_1 \phi_2 & 2m_2^2 + \lambda_2 \phi_2^2 + (\lambda_3 + \lambda_4 - \lambda_5)\phi_1^2 \end{pmatrix}. \tag{7}$$

By taking $\phi_i = v_i$ and diagonalizing these matrices, the physical masses of the charged scalar field $H^\pm$ and the neutral CP-odd scalar field A are respectively obtained as

$$m_{H^\pm}^2 = \frac{m_3^2}{\sin\beta \cos\beta} - \frac{1}{2}(\lambda_4 + \lambda_5) v^2, \qquad m_A^2 = \frac{m_3^2}{\sin\beta \cos\beta} - \lambda_5 v^2, \tag{8}$$

where we have introduced the angle β as $\tan\beta \equiv v_2/v_1$. On the other hand, the physical squared masses of the neutral CP-even scalar fields H and h can be derived by diagonalizing the mass

Table 1. The four types of 2HDMs distinguished by Z_2 charges for each of the fermions.

	Φ_1	Φ_2	u_R	d_R	l_R	Q_L, L_L
Type I	+	−	−	−	−	+
Type II	+	−	−	+	+	+
Type X	+	−	−	−	+	+
Type Y	+	−	−	+	−	+

matrix

$$\mathcal{M}_h^2 = \frac{1}{2}\begin{pmatrix} 2m_1^2 + 3\lambda_1\phi_1^2 + (\lambda_3+\lambda_4+\lambda_5)\phi_2^2 & -2m_3^2 + 2(\lambda_3+\lambda_4+\lambda_5)\phi_1\phi_2 \\ -2m_3^2 + 2(\lambda_3+\lambda_4+\lambda_5)\phi_1\phi_2 & 2m_2^2 + 3\lambda_2\phi_2^2 + (\lambda_3+\lambda_4+\lambda_5)\phi_1^2 \end{pmatrix}, \tag{9}$$

with $\phi_i = v_i$, as

$$\begin{pmatrix} m_H^2 & 0 \\ 0 & m_h^2 \end{pmatrix} = R(-\alpha)\mathcal{M}_h^2 R(\alpha), \qquad R(\alpha) \equiv \begin{pmatrix} \cos\alpha & -\sin\alpha \\ \sin\alpha & \cos\alpha \end{pmatrix}. \tag{10}$$

Here, the squared masses m_H^2 and m_h^2 are obtained by

$$m_H^2 = \frac{1}{2}\left[A + C + \sqrt{(A-C)^2 + 4B^2}\right], \qquad m_h^2 = \frac{1}{2}\left[A + C - \sqrt{(A-C)^2 + 4B^2}\right], \tag{11}$$

with

$$A = m_3^2 \tan\beta + \lambda_1 v^2 \cos^2\beta, \tag{12}$$

$$B = -m_3^2 + (\lambda_3+\lambda_4+\lambda_5)v^2 \sin\beta\cos\beta, \tag{13}$$

$$C = \frac{m_3^2}{\tan\beta} + \lambda_2 v^2 \sin^2\beta. \tag{14}$$

Throughout this paper we take h as the SM-like Higgs boson with $m_h = 125\,\text{GeV}$.

The field-dependent masses of the W boson, the Z boson, and the photon can be written as

$$m_W = \frac{1}{2}g\sqrt{\phi_1^2+\phi_2^2}, \qquad m_Z = \frac{1}{2}\sqrt{g^2+g'^2}\sqrt{\phi_1^2+\phi_2^2}, \qquad m_\gamma = 0, \tag{15}$$

where g and g' are the gauge couplings of $SU(2)_L$ and $U(1)_Y$ gauge symmetry, respectively. The physical masses of the gauge bosons are derived by taking $\phi_i = v_i$.

The most general Yukawa term is

$$\mathcal{L}_{\text{Yukawa}} = -\bar{Q}_L Y_u \tilde{\Phi}_u u_R - \bar{Q}_L Y_d \Phi_d d_R - \bar{L}_L Y_l \Phi_l l_R + \text{h.c.}, \tag{16}$$

where Q_L and L_L are $SU(2)_L$ doublets of quarks and leptons, respectively, Y_f ($f = u, d, l$) are the Yukawa matrices of the fermions, and each of Φ_f is either Φ_1 or Φ_2. Since 2HDMs have two $SU(2)$ scalar doublets, we assume one of the doublets couples each of the fermions to avoid the tree-level flavor-changing neutral current. One of the ways to accomplish this is by assuming that 2HDMs have a Z_2 symmetry. In this case, there are four types in 2HDMs distinguished by the Z_2 charges for each of the fermions, as shown in Table 1 [79–81]. In a Type I 2HDM, all quarks and charged leptons obtain their masses from the VEV of Φ_2. In a Type II 2HDM, the VEV of Φ_2 gives the masses of the up-type quarks, while that of Φ_1 provides those of the down-type quarks and the charged leptons. In a Type X 2HDM, the charged leptons and quarks obtain their masses from the VEV of Φ_1 and Φ_2, respectively. In a Type Y 2HDM, the masses of the down-type quarks are generated by the VEV of Φ_1, while those of the up-type

quarks and the charged leptons are obtained by the VEV of Φ_2. The field-dependent masses of the fermions can be described as

$$m_f = \frac{1}{\sqrt{2}} y_f \phi_i, \tag{17}$$

where the value assigned to i depends on the types of Yukawa interactions. The physical masses of the fermions are obtained by taking $\phi_i = v_i$.

3. The effective potential at finite temperature

3.1 *The one-loop corrected effective potential*

An EWPT is caused by the temperature change of the effective scalar potential. To study the PT, we consider the thermal effective potential. The one-loop corrected effective potential at the finite temperature V^β is

$$V^\beta = V_0 + V_{\rm CW} + V_{\rm CT} + \overline{V}_1^\beta, \tag{18}$$

where V_0, $V_{\rm CW}$, $V_{\rm CT}$, and $\overline{V}_1^\beta$ are the tree-level potential in Eq. (4), the one-loop level potential at zero temperature (the Coleman–Weinberg potential), the counterterm potential, and the one-loop level potential at the finite temperature, respectively. The Coleman–Weinberg potential in the $\overline{\rm MS}$ scheme is written by [82]

$$V_{\rm CW}(\phi_1, \phi_2) = \pm \frac{1}{64\pi^2} \sum_k n_k m_k^4(\phi_1, \phi_2) \left[\log \frac{m_k^2(\phi_1, \phi_2)}{\mu^2} - c_k \right], \tag{19}$$

where k indicates scalar and gauge bosons and fermions, and n_k, m_k, and μ are the degrees of freedom of each field, the field-dependent mass of each field, and the renormalization scale which we set $\mu = 246\,\text{GeV}$, respectively. The upper (lower) sign corresponds to the bosonic (fermionic) contribution. The corresponding degrees of freedom are $n_k = 2, 1, 1, 1, 6, 3, 2, 12, 12$, and 4 for $k = H^\pm, H, h, A, W, Z, \gamma, t, b$, and τ, respectively. We only consider the fermions which have non-negligible contributions. The constants c_k are equal to 1/2 for transverse gauge bosons and 3/2 for the other particles in the $\overline{\rm MS}$ scheme.

$V_{\rm CW}$ changes the coordinate of the global minimum of the potential from that of V_0. We introduce the counterterm potential $V_{\rm CT}$ to fix the coordinate, the masses, and the mixing angles of the scalar fields to be equal to the tree-level ones. Thus, we impose the following five conditions to determine $V_{\rm CT}$:

$$\begin{aligned}
\left.\frac{\partial V_{\rm CT}(\phi_1,\ \phi_2)}{\partial \phi_i}\right|_{(\phi_1,\phi_2)=(v_1,v_2)} &= -\left.\frac{\partial V_{\rm CW}(\phi_1,\ \phi_2)}{\partial \phi_i}\right|_{(\phi_1,\phi_2)=(v_1,v_2)}, \\
\left.\frac{\partial^2 V_{\rm CT}(\phi_1,\ \phi_2)}{\partial \phi_i \partial \phi_j}\right|_{(\phi_1,\phi_2)=(v_1,v_2)} &= -\left.\frac{\partial^2 V_{\rm CW}(\phi_1,\ \phi_2)}{\partial \phi_i \partial \phi_j}\right|_{(\phi_1,\phi_2)=(v_1,v_2)} \qquad (i, j = 1, 2).
\end{aligned} \tag{20}$$

Following Ref. [16], we set $V_{\rm CT}$ with five parameters, δm_1^2, δm_2^2, $\delta\lambda_1$, $\delta\lambda_2$, and $\delta\lambda_{345}$:

$$V_{\rm CT} = \delta m_1^2 \phi_1^2 + \delta m_2^2 \phi_2^2 + \delta\lambda_1 \phi_1^4 + \delta\lambda_2 \phi_2^4 + \delta\lambda_{345} \phi_1^2 \phi_2^2. \tag{21}$$

Hence, the conditions in Eq. (20) give

$$\begin{aligned}
\delta m_1^2 &= -\frac{3}{4v_1} V_1 + \frac{1}{4} V_{11} + \frac{1}{4}\frac{v_2}{v_1} V_{12}, \quad \delta m_2^2 = -\frac{3}{4v_2} V_2 + \frac{1}{4} V_{22} + \frac{1}{4}\frac{v_1}{v_2} V_{12}, \\
\delta\lambda_1 &= \frac{1}{8v_1^3}(V_1 - v_1 V_{11}), \quad \delta\lambda_2 = \frac{1}{8v_2^3}(V_2 - v_2 V_{22}), \\
\delta\lambda_{345} &= -\frac{V_{12}}{4v_1 v_2},
\end{aligned} \tag{22}$$

where $V_i \equiv \partial V_{\rm CW}/\partial\phi_i|_{(v_1,v_2)}$ and $V_{ij} \equiv \partial^2 V_{\rm CW}/(\partial\phi_i\partial\phi_j)\big|_{(v_1,v_2)}$. We calculate δm_1^2, δm_2^2, $\delta\lambda_1$, $\delta\lambda_2$, and $\delta\lambda_{345}$ numerically and substitute them into $V_{\rm CT}$. However, there are infrared divergences in the second derivatives of $V_{\rm CW}$ that are proportional to $\log m_{\rm NG}^2$, where $m_{\rm NG}$ indicate the masses of the Nambu–Goldstone (NG) bosons. To avoid these divergences we use the approximation shown in Ref. [83], where $m_{\rm NG}$ is approximated as the mass of the SM-like Higgs boson, i.e. $m_{\rm NG} \to m_h$. This approximation is justified because the divergences are only logarithmic, hence changing the masses of the NG bosons does not make a large difference.

The one-loop thermal contributions to the potential can be written as [84]

$$\overline{V}_1^{\beta}(\phi_1,\phi_2) = \pm\frac{T^4}{2\pi^2}\sum_k \int dx\, x^2 \ln\left[1 \mp \exp\left(-\sqrt{x^2 + \frac{m_k^2(\phi_1,\phi_2)}{T^2}}\right)\right], \tag{23}$$

where T represents the temperature and the upper (lower) sign indicates the bosonic (fermionic) contribution. We calculate the integral in Eq. (23) numerically. The squared masses of the scalar bosons in Eq. (23) can become negative for certain sets of the coordinates (ϕ_1, ϕ_2) and T.[4] In that case, we adopt the method of discarding the imaginary part of the thermal potential, which is related to the instability of the field configuration [85], and taking only the real part (see, e.g., Ref. [15]).

3.2 *Resummation*

Although V^{β} contains the corrections to the one-loop level, the contributions of higher-loop diagrams get larger as the temperature rises. The dominant diagrams at high temperatures are called daisy diagrams [84]. We perform resummation, which is the method for taking into account the corrections from the diagrams [86,87]. There are two methods of resummation; we apply the Parwani method [86].[5] The resummation is achieved by appending the corrections from the scalar and gauge boson polarization tensors in the infrared limit $\Pi_B(T)$ to the boson masses m_B^2,

$$m_B^2(\phi_1,\phi_2) \to m_B^2(\phi_1,\phi_2) + \Pi_B(T), \tag{24}$$

and inserting these corrected masses into $\overline{V}_1^{\beta}$ in Eq. (23) [89]. The index B represents the boson species.

In 2HDMs, we carry out the resummation concretely as follows. The resummation for scalar fields is performed by adding the contributions of the two-point functions to the mass parameters $m_{\,1}$ and $m_{\,2}$ in the mass matrices of Eqs. (7) and (9) [90],

$$m_i^2 \to m_i^2 + c_i T^2, \tag{25}$$

[4] We comment on the region for negative scalar squared masses in Appendix A. Negative quadratic parameters sometimes yield negative squared masses at finite temperature; this is discussed in connection with the region involved in Fig. 4.

[5] The other method of resummation is called the Arnold–Epinosa (AE) method [87]. This takes into account only bosonic Matsubara zero modes which are involved in infrared divergences and adds cubic terms to the potential. The procedure uses the high-temperature expansion when dividing the thermal contributions into those of the zero and non-zero modes. Hence, it would be unsuccessful in regions where the high-temperature expansion is not valid. In our calculation of the multi-step EWPT, we need to consider the PT near the EW vacuum in some cases (cf. Fig. 5), where the high-temperature expansion is broken because the condition of the expansion, $m_B/T < 1$, would not be satisfied. Therefore, the AE method is not suitable for the computation of the multi-step EWPT. In contrast to the AE method, the Parwani method can take the non-relativistic limit smoothly even if theories include heavy particles [83,88] since the method does not contain the high-temperature expansion.

where the c_i are the coefficients of correction terms and are determined by $\Pi_B(T)$, which depends on the types of Yukawa interactions. In the Type I 2HDM they can be written by [16]

$$c_1 = \frac{1}{8}g^2 + \frac{1}{16}(g^2 + g'^2) + \frac{1}{4}\lambda_1 + \frac{1}{6}\lambda_3 + \frac{1}{12}\lambda_4,$$
$$c_2 = \frac{1}{8}g^2 + \frac{1}{16}(g^2 + g'^2) + \frac{1}{4}\lambda_2 + \frac{1}{6}\lambda_3 + \frac{1}{12}\lambda_4 + \frac{1}{4}y_t^2 + \frac{1}{4}y_b^2 + \frac{1}{12}y_\tau^2. \tag{26}$$

For the other Yukawa types, one can obtain the coefficients by apportioning the Yukawa coupling terms in Eq. (26) to c_1 and c_2 according to Table 1. We then append the correction terms to the non-diagonalized scalar matrices $\mathcal{M}^2_{w^\pm}$, $\mathcal{M}^2_z$, and $\mathcal{M}^2_h$ in Eqs. (7) and (9) as

$$\mathcal{M}^2_{w^\pm} + \begin{pmatrix} c_1 & 0 \\ 0 & c_2 \end{pmatrix} T^2, \qquad \mathcal{M}^2_z + \begin{pmatrix} c_1 & 0 \\ 0 & c_2 \end{pmatrix} T^2, \qquad \mathcal{M}^2_h + \begin{pmatrix} c_1 & 0 \\ 0 & c_2 \end{pmatrix} T^2, \tag{27}$$

and obtain the corrected scalar masses by diagonalizing them. For the gauge fields, one can carry out the resummation by appending the contributions to only the longitudinal component of the mass matrices. Following Ref. [90], the corrected masses of the longitudinal W boson can be written by

$$M^2_{W_L} = \frac{g^2}{4}\left(\phi_1^2 + \phi_2^2\right) + 2g^2T^2. \tag{28}$$

The corrected mass matrix of the longitudinally polarized Z boson and photon in the gauge basis is

$$\frac{1}{4}(\phi_1^2 + \phi_2^2)\begin{pmatrix} g^2 & -gg' \\ -gg' & g'^2 \end{pmatrix} + \begin{pmatrix} 2g^2T^2 & 0 \\ 0 & 2g'^2T^2 \end{pmatrix}. \tag{29}$$

By diagonalizing it, the corrected masses of the Z boson and the photon are obtained as

$$M^2_{Z_L} = \frac{1}{8}\left(g^2 + g'^2\right)\left(\phi_1^2 + \phi_2^2 + 8T^2\right) + \Delta,$$
$$M^2_{\gamma_L} = \frac{1}{8}\left(g^2 + g'^2\right)\left(\phi_1^2 + \phi_2^2 + 8T^2\right) - \Delta, \tag{30}$$

with

$$\Delta = \left\{\left[\frac{1}{8}\left(g^2 + g'^2\right)\left(\phi_1^2 + \phi_2^2 + 8T^2\right)\right]^2 - g^2g'^2T^2\left(\phi_1^2 + \phi_2^2 + 4T^2\right)\right\}^{1/2}. \tag{31}$$

4. Theoretical constraints and EW vacuum stability

For the theoretical constraints on the model we consider constraints from the boundedness from below (BFB) of V_0, which is described as [91–94]

$$\lambda_1 > 0, \qquad \lambda_2 > 0, \qquad -\sqrt{\lambda_1\lambda_2} < \lambda_3, \qquad -\sqrt{\lambda_1 + \lambda_2} < \lambda_3 + \lambda_4 - \lambda_5; \tag{32}$$

the perturbativity,

$$|\lambda_n| < 4\pi \qquad (n = 1, 2, \ldots, 5); \tag{33}$$

and the tree-level unitarity [95,96].

Furthermore, absolute tree-level stability of the EW vacuum is required [97, 98], where a negative m_3^2 is disfavored. In the following analyses, we confirm numerically that the EW vacuum is the global minimum in the region for $|\phi_i| \leq 10\,\text{TeV}$, and remove the cases where $\sqrt{\phi_1^2 + \phi_2^2} = 246\,\text{GeV}$ is not satisfied at the global minimum.

5. Numerical results

In this section we discuss the parameter space where the multi-step PT occurs. To study the PT, CosmoTransitions [99] is used in the analyses. We also study the region where the strongly first-order PT occurs in a multi-step PT. The strength of the PT ξ is defined by

$$\xi \equiv \frac{v_c}{T_c}, \tag{34}$$

where T_c is the critical temperature at which minima degenerate between two phases, and v_c is the critical value of $\sqrt{\phi_1^2 + \phi_2^2}$ at T_c. As the criterion for a strong PT we consider $\xi \geq 1$, where the sphaleron processes are suppressed enough in the $SU(2)$ broken phase. We especially focus on the cases where the first step of a two-step PT is strongly first order,[6] which we name "strong two-step PTs."[7] In this case the sphaleron rate is suppressed in the broken phase, and it is expected that v_c and T_c at subsequent PT steps are respectively larger and smaller than the previous PT. Therefore, the inequality $\xi \geq 1$ is kept and the sphaleron rate is also suppressed at the subsequent PT steps.[8]

In the following analysis, instead of the eight parameters ($m_1^2, m_2^2, m_3^2, \lambda_{1-5}$) in V_0 we take the following set as the input parameters:

$$m_{H^\pm}, \quad m_A, \quad m_H, \quad \tan\beta, \quad \cos(\beta-\alpha), \quad m_3, \quad m_h, \quad v. \tag{35}$$

Here, $m_h = 125\,\text{GeV}$ and $v = 246\,\text{GeV}$. In order to put restrictions on the ranges of the other input parameters, we consider the experimental constraints from EW precision data, $B \to X_s\gamma$ decays, $H^\pm \to \tau\nu$ decays, and the coupling measurements of the Higgs boson. The EW precision data can be satisfied by assuming mass degeneracy between the charged scalar boson and at least one of the extra neutral scalar bosons, $m_{H^\pm} \simeq m_A$ or m_H, which recovers the custodial symmetry and hence the parameter $\rho \simeq 1$, as in the SM [100]. For $m_{H^\pm}$, the range $m_{H^\pm} < 590\,\text{GeV}$ is excluded from $B \to X_s\gamma$ decays in Type II and Y 2HDMs [101], while $m_{H^\pm} \leq 170\,\text{GeV}$ is excluded from $H^\pm \to \tau\nu$ decays in Type X 2HDMs [102]. The constraints from the coupling measurements of the Higgs boson [103] show that, e.g., $|\cos(\beta-\alpha)| > 0.25$ (0.3) is excluded at $\tan\beta = 2$ (10) in Type I 2HDMs, and $|\cos(\beta-\alpha)| > 0.15$ (0.05) is excluded at $\tan\beta = 2$ (10) in Type X 2HDMs. The constraints for Type II and Y 2HDMs are stricter than those for Type I and X.

In our analyses, based on the above constraints, we take the ranges for the input parameters in Type I and X 2HDMs shown in Table 2. Imposing the mass degeneracy $m_\Phi = m_{H^\pm}$ ($\Phi = H$ or A), the ranges for m_A and m_H are taken as 180 GeV–1 TeV for m_Φ and 130 GeV–1 TeV for the other extra neutral scalar boson. For the mixing angles, we take $\tan\beta = 2$–10, and $|\cos(\beta-\alpha)| \leq 0.25$ in Type I 2HDMs, while the *alignment limit*, $\cos(\beta-\alpha) = 0$, in Type X 2HDMs. In the analyses we focus on relatively small values for m_3 as $0 \leq m_3 \leq 100\,\text{GeV}$, since the strong two-step PTs which we are interested in prefer to occur for smaller m_3 and do not occur for $m_3 \simeq 100\,\text{GeV}$ (cf. Fig. 6). As depicted in Table 2, we take every 10 GeV for m_A and m_H, 0.5 for

[6] We take into account the first-order, second-order, and cross-over PTs as first-step PTs.

[7] Strong three-step PTs (i.e. three-step PTs where the first-step PT is strongly first order) are found in Type I 2HDMs, where they occur in the region where strong two-step PTs happen. However, the number of points for such PTs is much smaller than that for the strong two-step PTs, and hence we do not discuss the results. Note that we cannot find such PTs in the Type X 2HDMs.

[8] If the baryon number is generated at the first-step PT (although our model cannot generate a baryon number since CP is conserved), it remains unwashed-out.

Table 2. Parameter regions studied in Type I and Type X 2HDMs with m_A or $m_H = m_{H^\pm}$. We perform analyses for every 10 GeV in the masses of the neutral scalar bosons, 0.5 in $\tan\beta$, 0.05 in $\cos(\beta-\alpha)$ (though we set $\cos(\beta-\alpha)=0$ in the Type X 2HDMs), and 5 GeV in m_3.

	m_A [GeV]	m_H [GeV]	$\tan\beta$	$\cos(\beta-\alpha)$	m_3 [GeV]
Type I ($m_A = m_{H^\pm}$)	180–1000 (/10)	130–1000 (/10)	2–10 (/0.5)	−0.25–0.25 (/0.05)	0–100
Type I ($m_H = m_{H^\pm}$)	130–1000 (/10)	180–1000 (/10)	2–10 (/0.5)	−0.25–0.25 (/0.05)	0–100
Type X ($m_A = m_{H^\pm}$)	180–1000 (/10)	130–1000 (/10)	2–10 (/0.5)	0	0–100
Type X ($m_H = m_{H^\pm}$)	130–1000 (/10)	180–1000 (/10)	2–10 (/0.5)	0	0–100

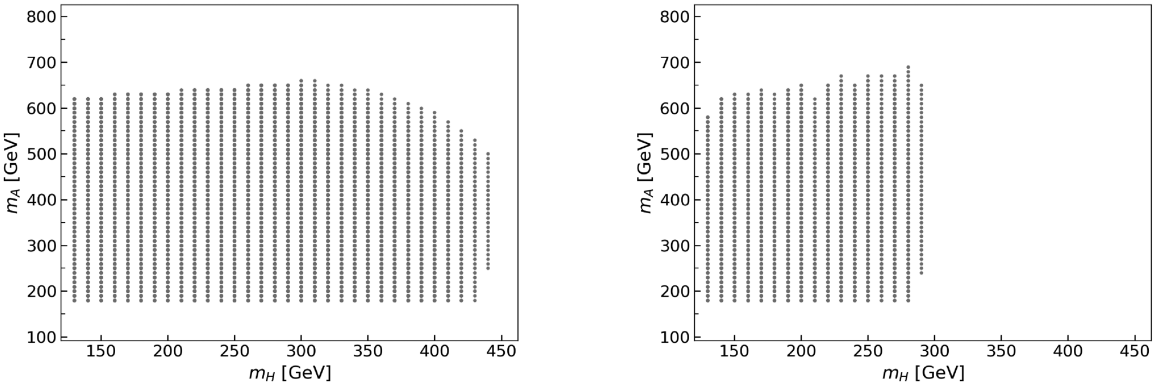

Fig. 1. Parameter regions in the m_A vs. m_H plane allowed by the theoretical constraints (BFB, perturbativity, and tree-level unitarity) in Type I 2HDMs with $m_A = m_{H^\pm}$. The left and right panels show the regions for $\tan\beta = 2$ and 7, respectively. The other input parameters follow Table 2.

$\tan\beta$, 0.05 for $\cos(\beta-\alpha)$ (though we set $\cos(\beta-\alpha)=0$ in the Type X 2HDMs), and 5 GeV for m_3 .

In the Type II and Y 2HDMs, we take the same ranges for the input parameters as for the Type X 2HDMs, but $m_\Phi = m_{H^\pm} \geq 590$ GeV by the constraint from $B \to X_s\gamma$. In these cases, we have found that the stability of the EW vacuum is not realized because the contributions of the heavy extra scalar fields lift up the potential significantly at the EW vacuum (see Eq. (19)) and the origin $(\phi_1, \phi_2) = (0, 0)$ becomes the global minimum. Hence, we discuss only Type I and X 2HDMs hereafter.

5.1 *Type I*

5.1.1 *Type I* ($m_A = m_{H^\pm}$). In this subsection we show the results for Type I 2HDMs with $m_A = m_{H^\pm}$. Figure 1 shows the parameter region allowed by the theoretical constraints (BFB, perturbativity, and tree-level unitarity) in the m_A vs. m_H plane at $\tan\beta = 2$ (left) and 7 (right). It shows that in the case of $\tan\beta = 7$ the upper limit on m_H is lower than for $\tan\beta = 2$, as $m_H \lesssim 290$ (440) GeV for $\tan\beta = 7$ (2).

The left panels of Fig. 2 show the parameter points where one-step and multi-step PTs (left) occur in the m_A vs. m_H (top), m_A vs. $\tan\beta$ (middle), and m_A vs. $\cos(\beta-\alpha)$ (bottom) planes. The yellow, blue, and purple points show the results for one-step, two-step, and three-or-more-

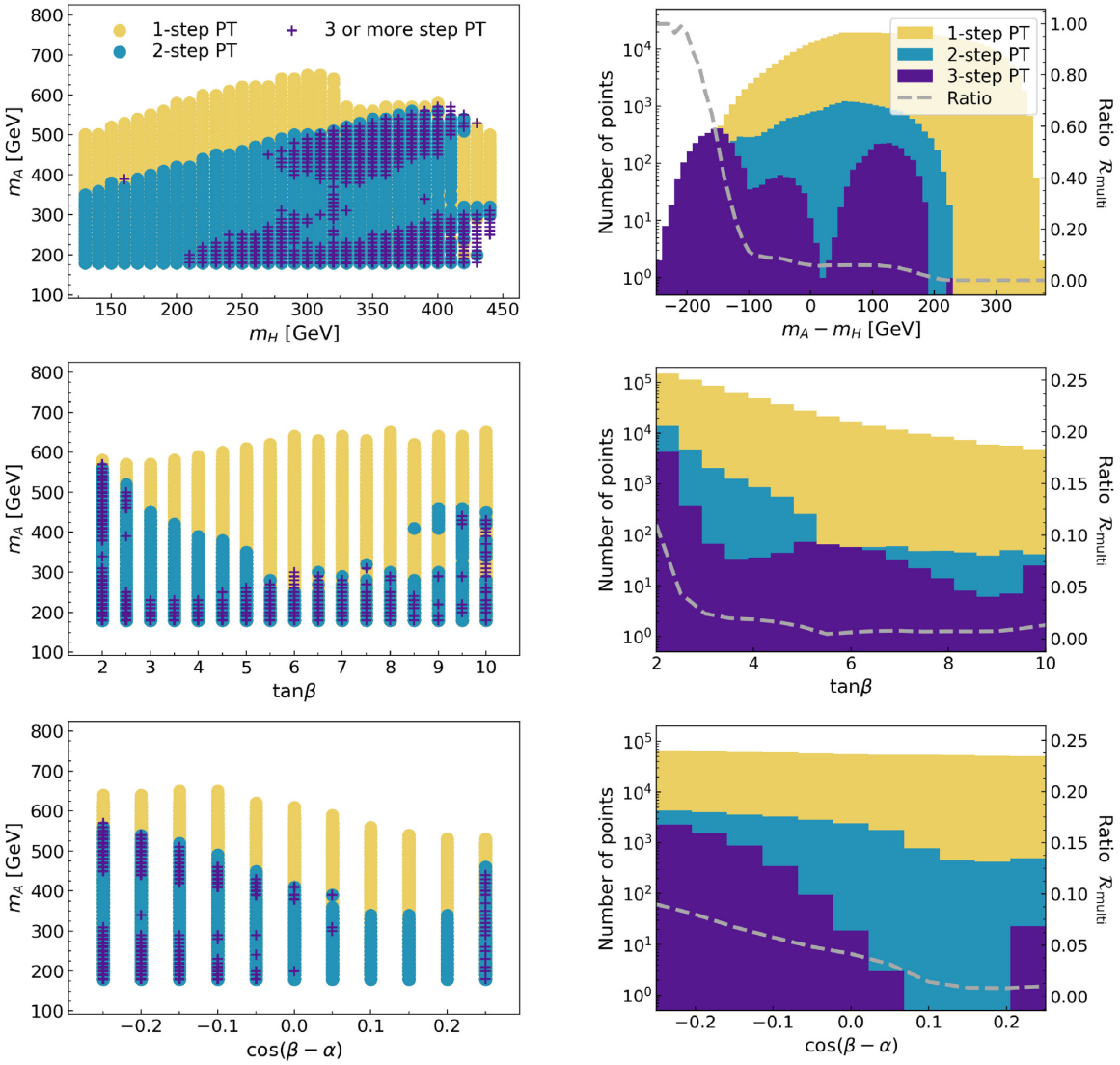

Fig. 2. Left: Parameter points where one-step and multi-step PTs occur in the m_A vs. m_H (top), m_A vs. $\tan\beta$ (middle), and m_A vs. $\cos(\beta-\alpha)$ (bottom) planes Type I 2HDMs with $m_A = m_{H^\pm}$. The yellow, blue, and purple points show the results for one-, two-, and three-or-more-step PTs, respectively. Right: Number of points where one-step and multi-step PTs occur as functions of $m_A - m_H$ (top), $\tan\beta$ (middle), and $\cos(\beta-\alpha)$ (bottom). The one-, two-, and three-or-more-step PTs are colored yellow, blue, and purple, respectively. The gray dashed lines represent $\mathcal{R}_{\rm multi}$, the ratio of the number of points for multi-step PTs to the number for all PTs.

step PTs, respectively. [9] Here, in addition to the theoretical constraints considered in Fig. 1, the constraint of the stability of the EW vacuum is further imposed. Comparing the top left panel in Fig. 2 with Fig. 1, we can see that the region with larger m_A (and m_H) is excluded by the constraint. In the left panels of Fig. 2, the range of m_A where multi-step PTs occur gets larger as m_H increases, and $\tan\beta$ and $\cos(\beta-\alpha)$ (except for $\tan\beta \simeq 10$ and $\cos(\beta-\alpha) \simeq 0.25$) respectively decrease. In the top left panel of Fig. 2, the parameter region for multi-step PTs overlaps with that of one-step PTs, but for the region where $m_H \simeq 420$ GeV with $m_A \simeq 550$ GeV or 200–300 GeV, three-or-more-step PTs occur the most. The right panels in Fig. 2 show the

[9] "Three-or-more-step PTs" includes four-step PTs. The numbers of points for three- and four-step PTs account for about 1% and 0.1% of all points in this case, respectively.

number of points for one-step (yellow), two-step (blue), and three-or-more-step (purple) PTs, respectively, as functions of $m_A - m_H$ (top), $\tan\beta$ (middle), and $\cos(\beta-\alpha)$ (bottom). The ratios $\mathcal{R}_{\rm multi}$ in the panels, plotted as gray dashed lines, are the ratios of the number of points for multi-step PTs to the number for all PTs,

$$\mathcal{R}_{\rm multi} = \frac{\#\text{ of points for multistep PTs}}{\#\text{ of points for all PTs}}. \tag{36}$$

We see in the top right panel of Fig. 2 that multi-step PTs favor $m_A - m_H < 0$, and the ratio $\mathcal{R}_{\rm multi} \simeq 1$ is obtained at $m_A - m_H \simeq -210$ GeV. Hence, when $\mathcal{R}_{\rm multi}$ becomes around 1, $m_H \gtrsim 390$ GeV and m_A is around 200 GeV. Moreover, the middle and bottom right panels of Fig. 2 show that $\mathcal{R}_{\rm multi}$ becomes larger for smaller $\tan\beta$ and $\cos(\beta-\alpha)$, and reaches about 10% at $\tan\beta = 2$ and $\cos(\beta-\alpha) = -0.25$, respectively. For $\tan\beta \simeq 10$ and $\cos(\beta-\alpha) \simeq 0.25$, we can see that $\mathcal{R}_{\rm multi}$ is only a few percent, although the allowed ranges of m_A for multi-step PTs are wide in the middle and bottom left panels of Fig. 2.

As expected from Fig. 1, the regions with $m_H \simeq 420$ GeV are realized for $\tan\beta \simeq 2$ in this analysis. In such a low-$\tan\beta$ case, the $B \to \mu^+\mu^-$ process gives the constraint on $m_{H^\pm}$ as, e.g., $m_{H^\pm} > 340$ (125) GeV at $\tan\beta \simeq 2$ (3) at 95 %CL for Type I and X 2HDMs [101]. Therefore, the region where three-or-more-step PTs occur the most with $m_H \simeq 420$ GeV and $m_A\ (= m_{H^\pm}) \simeq 200$–$300$ GeV is excluded by the constraint from $B \to \mu^+\mu^-$. We have found that even when the constraint is taken into account in this analysis, the multi-step PTs favor the mass hierarchy $m_A < m_H$ and, e.g., $\mathcal{R}_{\rm multi} \simeq 100\%$ (10%) is obtained at $m_A - m_H \simeq -150$ (-80) GeV. Moreover, we should note that if $m_A - m_H < -m_Z$, the region would be constrained by the extra Higgs boson search $H \to AZ$ at the LHC [104–106]. It is generally more severe for low $\tan\beta$ and $\cos(\beta-\alpha)$ closer to zero [107, 108]. We leave the detailed analyses including the constraints from such extra Higgs boson searches for future work.

The left panels of Fig. 3 show the parameter points where the two-step and strong two-step PTs occur in the m_A vs. m_H (top), m_A vs. $\tan\beta$ (middle), and m_A vs. $\cos(\beta-\alpha)$ (bottom) planes as in Fig. 2. The blue and dark-blue points represent the parameter points where two-step and strong two-step PTs occur, respectively. From the top left panel of Fig. 3, we can see that strong two-step PTs happen in the region where $m_A \gtrsim 300$ GeV and $m_H \lesssim 350$ GeV, and the mass hierarchy $m_A > m_H$ exists. Additionally, in the middle and bottom left panels of Fig. 3, the range of m_A where strong two-step PTs happen increases as $\tan\beta$ and $\cos(\beta-\alpha)$ become smaller. Here, the strong two-step PTs occur only for $\tan\beta \lesssim 5$. The right panels in Fig. 3 show the number of points for two-step (blue) and strong two-step PTs (dark-blue), respectively, as functions of $m_A - m_H$ (top), $\tan\beta$ (middle), and $\cos(\beta-\alpha)$ (bottom). The ratios $\mathcal{R}_{\rm st2}$ in the right panels are the ratios of the number of points for strong two-step PTs to the number for two-step PTs,

$$\mathcal{R}_{\rm st2} = \frac{\#\text{ of points for strong twostep PTs}}{\#\text{ of points for twostep PTs}}, \tag{37}$$

which are shown by green dashed lines. It is notable that in the top right panel of Fig. 3 the strong two-step PTs favor $m_A - m_H > 0$ and $\mathcal{R}_{\rm st2}$ becomes $\mathcal{R}_{\rm st2} = 100\%$ at $m_A - m_H \simeq 210$ GeV. Moreover, the strong two-step PTs are likely to occur at small $\tan\beta$ and $\cos(\beta-\alpha)$, as shown in the middle and bottom right panels of Fig. 3. The parameter regions for strong two-step PTs do not receive the constraint from $B \to \mu^+\mu^-$, while some of them with $m_A - m_H > m_Z$ could be constrained from the $A \to HZ$ decay at the LHC [107,108] .

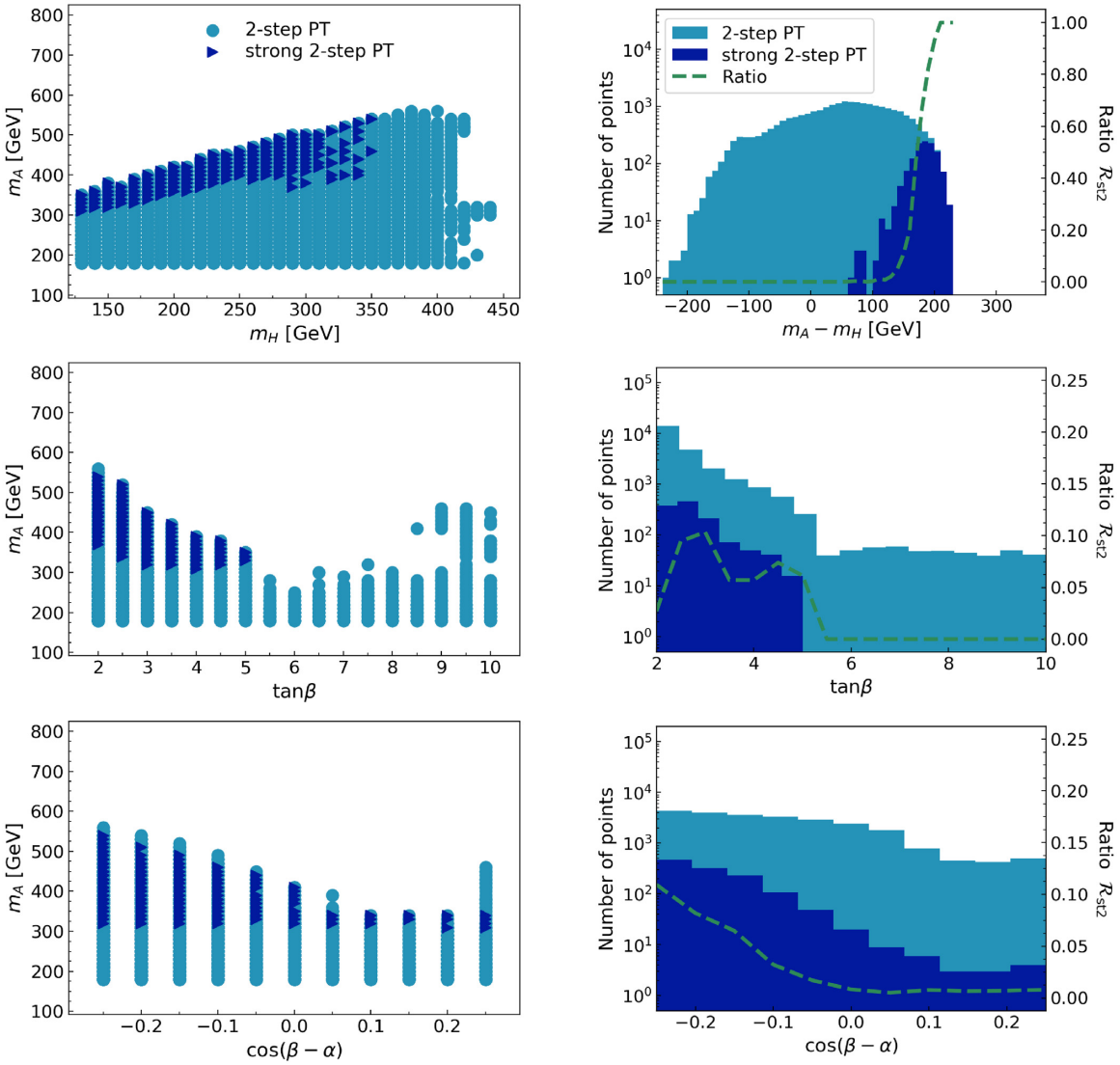

Fig. 3. Left: Parameter points where two-step and strong two-step PTs occur in the m_A vs. m_H (top), m_A vs. $\tan\beta$ (middle), and m_A vs. $\cos(\beta-\alpha)$ (bottom) planes for Type I 2HDMs with $m_A = m_{H^\pm}$. The blue and dark-blue points represent the parameter points where two-step and strong two-step PTs occur, respectively. Right: Number of points where two-step and strong two-step PTs occur as functions of $m_A - m_H$ (top), $\tan\beta$ (middle), and $\cos(\beta-\alpha)$ (bottom). The two-step and strong two-step PTs are colored blue and dark blue, respectively. The green dashed lines represent $\mathcal{R}_{\rm st2}$, the ratio of the number of points for strong two-step PTs to the number for two-step PTs.

Multi-step PTs tend to occur for smaller $\tan\beta$ and $\cos(\beta-\alpha)$. Next, we investigate the correlations between these parameters and m_2^2, an important parameter in determining the path of a PT. As we will see later in Fig. 5, the VEVs after the first step in multi-step PTs have a tendency to be located mainly along the ϕ_2 axis. We therefore expect that m_2^2 should be negative and have a large enough magnitude to make multi-step PTs occur, because such an m_2^2 makes the potential decrease in the direction of the ϕ_2 axis. From Eq. (6), m_2^2 can be written as

$$m_2^2 = \frac{1}{\tan\beta}\left[m_3^2 - \frac{1}{2}\left(m_H^2 - m_h^2\right)\cos\alpha\sin\alpha\right] - \frac{1}{2}\left(m_h^2\cos^2\alpha + m_H^2\sin^2\alpha\right). \tag{38}$$

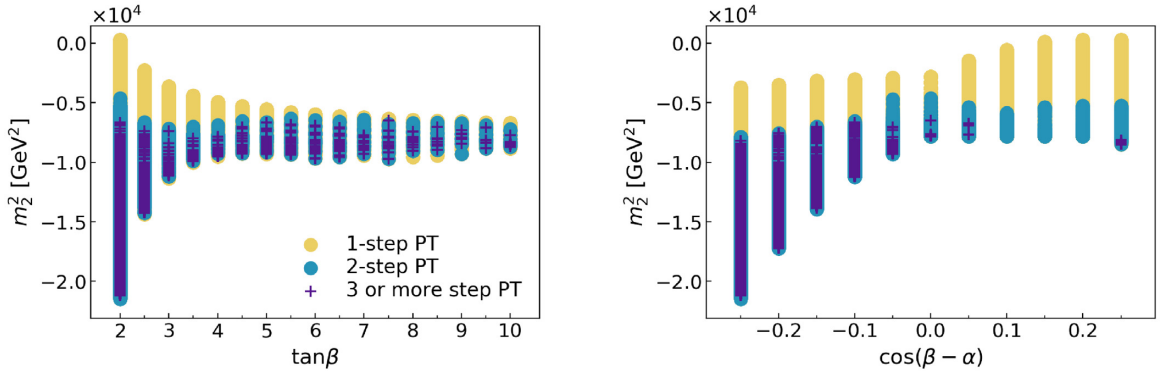

Fig. 4. Parameter points where one-step, two-step, and three-or-more-step PTs occur in the m_2^2 vs. $\tan\beta$ (left) and m_2^2 vs. $\cos(\beta-\alpha)$ (right) planes for Type I 2HDMs with $m_A = m_{H^\pm}$.

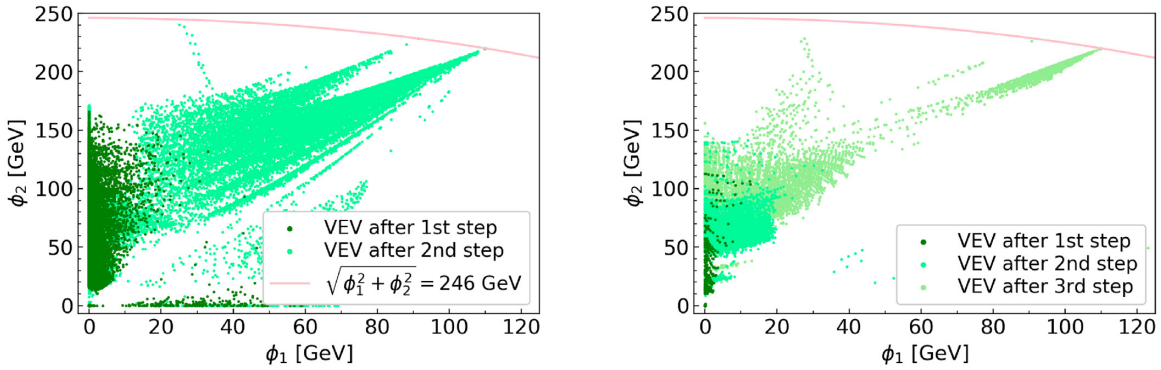

Fig. 5. VEVs after each step of a two-step (left) and three-step (right) PT in a Type I 2HDM with $m_A = m_{H^\pm}$. The dark-green, green, and light-green points represent the VEVs after the first-, second-, and third-step PTs, respectively. The pink line represents the place where $\sqrt{\phi_1^2+\phi_2^2} = 246\,\text{GeV}$, on which the EW vacuum lies.

In Fig. 4, the regions where one-step, two-step, and three-or-more-step PTs occur are shown in the m_2^2 vs. $\tan\beta$ (left) and m_2^2 vs. $\cos(\beta-\alpha)$ (right) plane, respectively. As can be expected, multi-step PTs occur for smaller m_2^2 as $m_2^2 \lesssim -0.5\times10^4\,\text{GeV}^2$. The minimum value of m_2^2 decreases for smaller $\tan\beta$ and $\cos(\beta-\alpha)$. These features can be understood from Eq. (38). The leading term on the right-hand side of Eq. (38) is the last one, $-\frac{1}{2}m_H^2\sin^2\alpha$, in our explored parameter region. Hence, as $m_H|\sin\alpha|$ increases, a negative m_2^2 with a large magnitude can be obtained. As shown in Fig. 1, a larger m_H is allowed for smaller $\tan\beta$. On the other hand, $|\sin\alpha|$ increases as $\cos(\beta-\alpha)$ gets smaller in our parameter space. Thus, the minimum value of m_2^2 decreases as $\tan\beta$ and $\cos(\beta-\alpha)$ get smaller. Meanwhile, at $\cos(\beta-\alpha)\simeq0.2$, $\sin\alpha$ can be zero. In this case, the second and last terms in Eq. (38) vanish and the value of m_H does not affect m_2^2. However, in the region where $\cos(\beta-\alpha)\simeq0.25$ and $\tan\beta\simeq10$, $|\sin\alpha|$ can be large to some extent and the contribution of the last term in Eq. (38) recovers, which leads to a negative m_2^2 with a slightly large magnitude. This case is presented in Fig. 4.

As described above, when m_2^2 is negative with a large magnitude, the first step in a multi-step PT tends to occur along the ϕ_2 axis. In order to see this more clearly, we show in Fig. 5 the VEVs after each step of a two-step (left) and three-step (right) PT in the ϕ_2 vs. ϕ_1 plane. The dark-green points indicate the VEVs after the first-step PTs, and the green points show them after the second-step PTs. In the right panel of Fig. 5, the light-green points indicate the VEVs

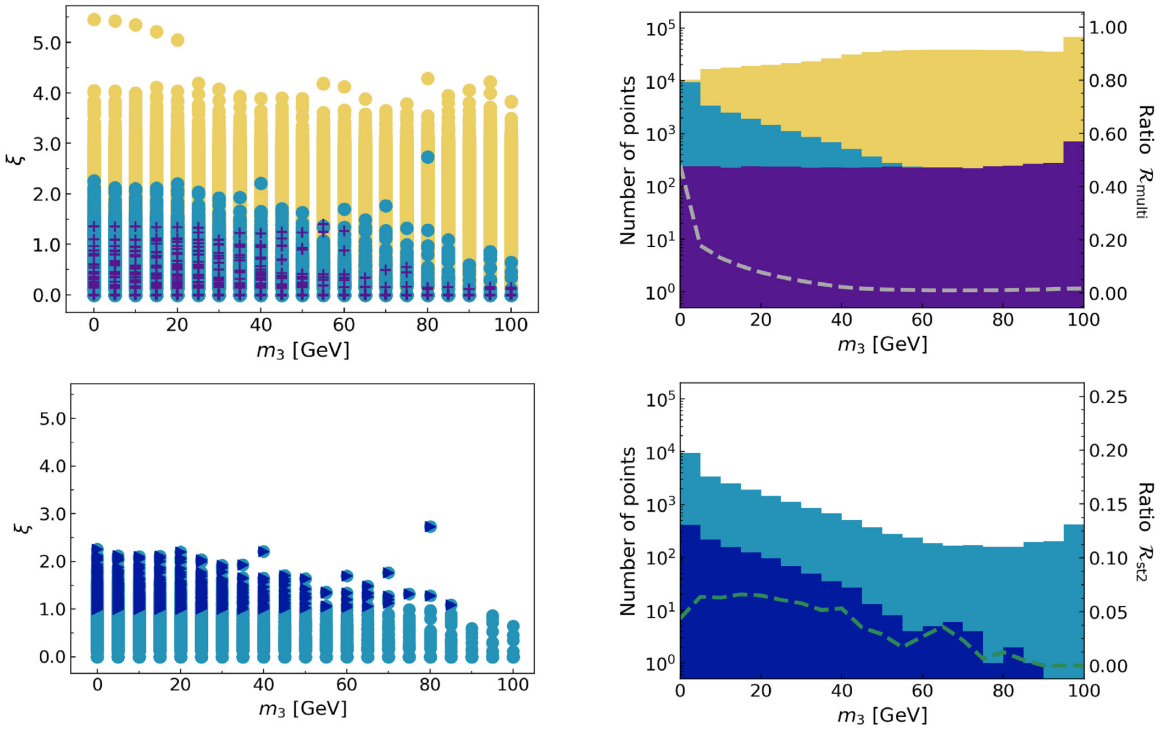

Fig. 6. Left: Parameter points where one-step and multi-step PTs (upper), and strong two-step PTs (lower), occur in the ξ vs m_3 plane for Type I 2HDMs with $m_A = m_{H^\pm}$. Right: Number of points where one-step and multi-step PTs (upper), and strong two-step PTs (lower), occur as a function of m_3. The gray (upper) and green (lower) dashed lines represent $\mathcal{R}_{\rm multi}$ and $\mathcal{R}_{\rm st2}$, respectively. The color scheme is the same as in Fig. 2.

after the third-step PTs. The EW vacuum, where the relation $\sqrt{\phi_1^2 + \phi_2^2} = 246\,\text{GeV}$ is satisfied, is located on the pink line. One can see that the dark-green points have a tendency to be along the axes, and the most of VEVs after the last-step PTs are located in the direction of the EW vacuum. In the left panel of Fig. 5, the VEVs after the first-step PTs extend in the directions of the ϕ_1 or ϕ_2 axes, even though many of them extend to the ϕ_2 axis. We find that those cases have negative m_1^2 or m_2^2 with a large magnitude, as expected. Additionally, it is found that the VEVs after the first-step PTs are located on or near the ϕ_1 axis when $\tan\beta \simeq 2$, $\cos(\beta - \alpha)$ is large, and m_3 is near zero. On the other hand, for the three-step PTs in the right panel of Fig. 5, the VEVs after the first-step PTs favor going along the ϕ_2 axis rather than ϕ_1. The magnitudes of those VEVs after the first-step PTs are not so large, therefore it would be difficult for the first-step PT of a three-step PT to become strongly first order. Similar results are also seen for Type I 2HDMs with $m_H = m_{H^\pm}$ and Type X 2HDMs with m_A or $m_H = m_{H^\pm}$.

Finally, the left panels of Fig. 6 show the strength of PT ξ of a first-step PT as a function of m_3.[10] Considering the tree-level potential V_0 in Eq. (4), a large m_3^2 makes the potential decrease in the region far from the axes and the magnitude of the negative m_2^2 small (cf. Eq. (38)). These make the direction of the first-step PT toward the region far from the axes, so that it is difficult for a multi-step PT whose first-step PT occurs along the axes to happen. From

[10] In Ref. [15], ξ of a one-step PT is computed with the Parwani method. Compared with our result ($\xi \lesssim 6$, as shown in the upper left panel of Fig. 6), larger values of ξ such as $\xi \gtrsim 20$ were obtained; however, the explored parameter ranges in Ref. [15] were larger, e.g. $0 \le m_3^2 \le 5 \times 10^5\,\text{GeV}^2$ and $1 \le \tan\beta \le 35$ for Type I 2HDMs.

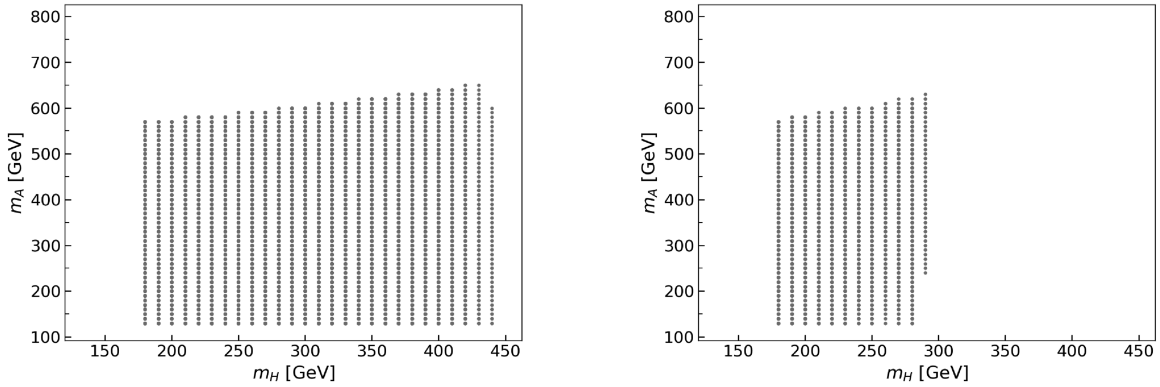

Fig. 7. Parameter regions in the m_A vs. m_H plane allowed by the theoretical constraints (BFB, perturbativity, and tree-level unitarity) for Type I 2HDMs with $m_H = m_{H^\pm}$. The left and right panels show the regions in the cases of $\tan\beta = 2$ and 7, respectively. The other input parameters follow Table 2.

the analysis, we have found that the maximum magnitude of the VEVs after the first step of a multi-step PT becomes gradually larger as m_3 gets smaller. Therefore, ξ of a first-step PT has a tendency to be large for smaller m_3. We have also found that larger $\mathcal{R}_{\rm multi}$ and $\mathcal{R}_{\rm st2}$ are obtained for smaller m_3, as in the right panels of Fig. 6. Note that no parameter points where strong two-step PTs occur were found for $m_3 \gtrsim 90$ GeV. We summarize in Tables B1 and B2 in Appendix B the values or ranges of input parameters where the ratios $\mathcal{R}_{\rm multi}$ and $\mathcal{R}_{\rm st2}$ have maximum values for Type I and X 2HDMs.

5.1.2 *Type I* ($m_H = m_{H^\pm}$). Figure 7 represents the parameter region allowed by the theoretical constraints (BFB, perturbativity, and tree-level unitarity) in the m_A vs. m_H plane at $\tan\beta = 2$ (left) and 7 (right) in Type I 2HDMs with $m_H = m_{H^\pm}$. We can see that the theoretical constraints on m_H at $\tan\beta = 7$ are more severe than at $\tan\beta = 2$, as $m_H \lesssim 290$ (440) GeV for $\tan\beta = 7$ (2).

Figure 8 shows the parameter points where the one-step, two-step, and three-or-more-step PTs (left) and the strong two-step PTs (right) occur for Type I 2HDMs with $m_H = m_{H^\pm}$ in the m_A vs. m_H (first line), m_A vs. $\tan\beta$ (second line), m_A vs. $\cos(\beta-\alpha)$ (third line), and ξ vs. m_3 (fourth line) planes, respectively. Here, the constraint from the stability of the EW vacuum is imposed. It is weaker than that for Type I 2HDMs with $m_A = m_{H^\pm}$, since the maximum mass scale of the extra scalar fields is lower due to the smaller maximal value of $m_{H^\pm}$ $(= m_H) <$ 450 GeV. The ranges of m_A where multi-step PTs occur are larger as $\tan\beta$ and $\cos(\beta-\alpha)$ decrease in the left panels of the second and third lines in Fig. 8. Here, the number of points where multi-step PTs occur for $\tan\beta \simeq 10$ and $\cos(\beta-\alpha) \simeq 0.25$ is found to be small, as for Type I with $m_A = m_{H^\pm}$. On the other hand, we can see from the upper three left panels of Fig. 8 that there is a region where only multi-step PTs occur for $m_A \gtrsim 600$ GeV and $m_H \gtrsim 410$ GeV with $\tan\beta \simeq 2$ and $\cos(\beta-\alpha) \simeq -0.25$. Such a region could be confirmed by the extra Higgs boson search for $A \to HZ$ at the LHC. In the bottom left panel of Fig. 8, the maximum value of ξ for a first-step PT increases as m_3 gets smaller and reaches around 2. Moreover, we have found that the ratio $\mathcal{R}_{\rm multi}$ has its maximum value when $m_A - m_H$ is negative with a large magnitude like -210 GeV as in Type I 2HDMs with $m_A = m_{H^\pm}$ (cf. Table B1 of Appendix B). Additionally, $\mathcal{R}_{\rm multi}$ has maximum values at $\tan\beta \simeq 2$, $\cos(\beta-\alpha) \simeq -0.25$, and $m_3 \simeq 0$.

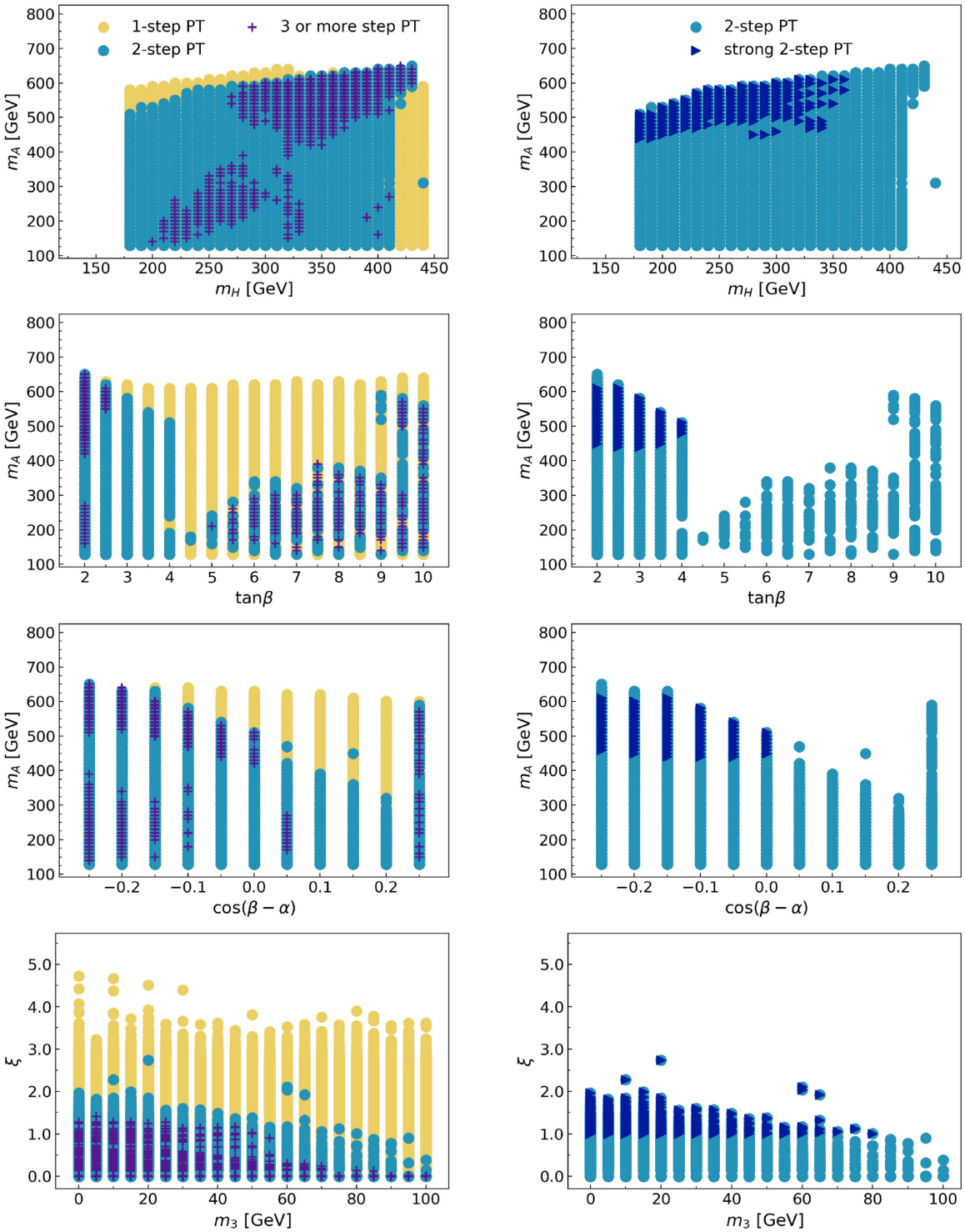

Fig. 8. As Figs. 2 and 6 but for Type I 2HDMs with $m_H = m_{H^\pm}$.

The strong two-step PTs occur for $m_A \gtrsim 440$ GeV and $m_H \lesssim 360$ GeV with the mass hierarchy $m_A > m_H$ in the top right panel of Fig. 8. We can also see that they happen only for $\tan\beta \lesssim 4$ and $\cos(\beta - \alpha) \lesssim 0$ from the right panels of the second and third lines. In addition, small m_3 is favored when strong two-step PTs happen in the bottom right panel. Some parameter points in the above region are excluded by the constraint from $B \to \mu^+\mu^-$, e.g. most of the points for

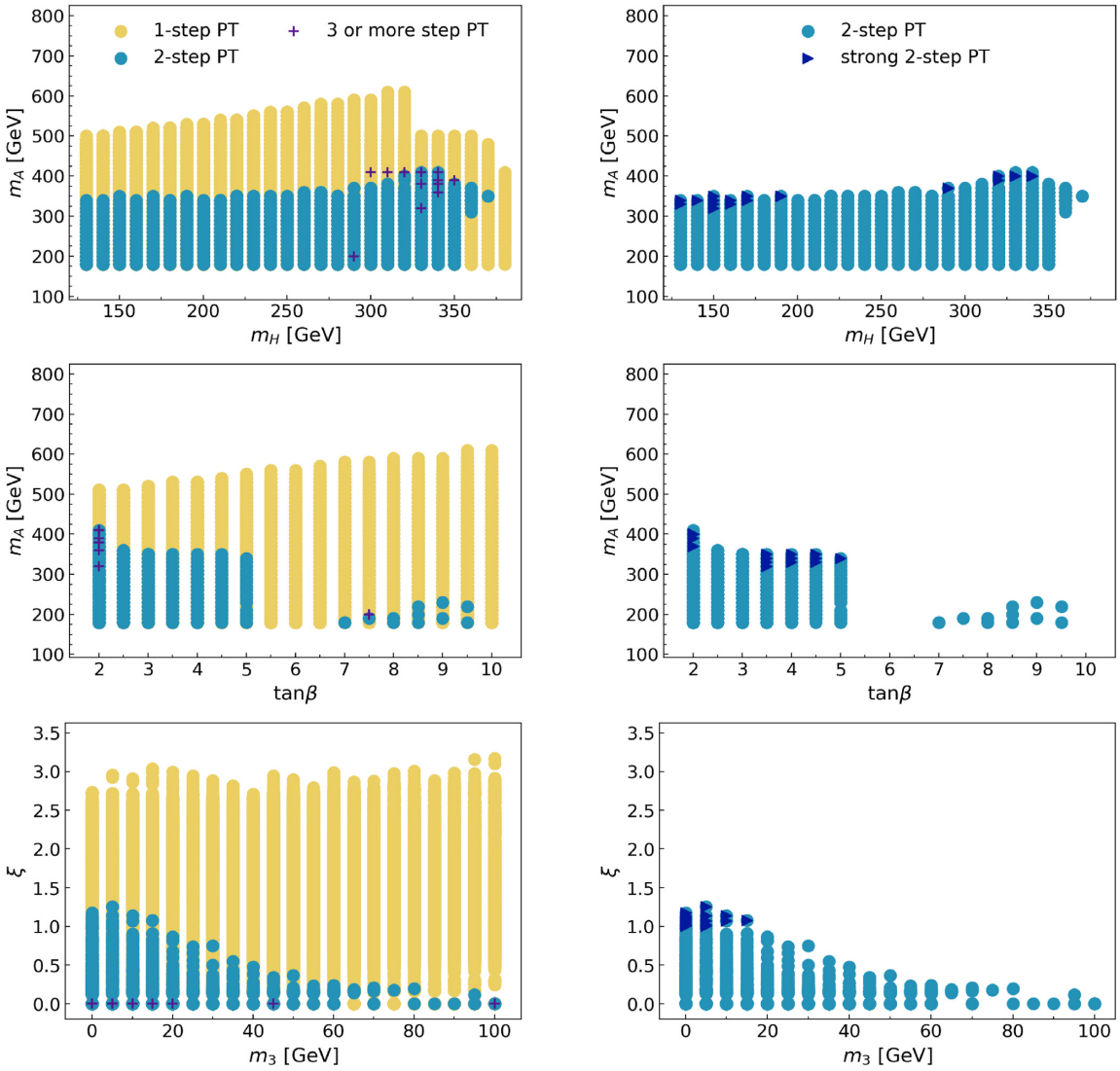

Fig. 9. Parameter points where one-step and multi-step PTs (left) and strong two-step PTs (right) occur in the m_A vs. m_H (top), m_A vs. $\tan\beta$ (middle), and ξ vs. m_3 (bottom) planes in Type X 2HDMs with $m_A = m_{H^\pm}$. The color scheme is as in Fig. 2. Note that we set $\cos(\beta - \alpha) = 0$.

multi-step PTs with $m_H \simeq 330$–340 GeV. Also, we have clarified that the ratio $\mathcal{R}_{\rm st2}$ is largest for $m_A - m_H > 0$ and small $\tan\beta$, $\cos(\beta - \alpha)$, and m_3, as shown in Table B2 of Appendix B. These tendencies are not changed even if we consider the constraint from $B \to \mu^+\mu^-$.

5.2 *Type X*

5.2.1 *Type X* ($m_A = m_{H^\pm}$). In the case of Type X 2HDMs, we take the alignment limit $\cos(\beta - \alpha) = 0$. Figure 9 presents the parameter points where one-step and multi-step PTs (left) and strong two-step PTs (right) occur in Type X 2HDMs with $m_A = m_{H^\pm}$ in the m_A vs. m_H (top), m_A vs. $\tan\beta$ (middle), and ξ vs. m_3 (bottom) planes.

In the top left panel of Fig. 9, the range of m_A where multi-step PTs occur does not change much for $m_H \lesssim 350$ GeV. The middle left panel shows that most multi-step PTs occur for $\tan\beta \lesssim 5$. From the bottom left panel, we can see that the maximum value of ξ for multi-step PTs increases as m_3 decreases and reaches around 1.2. From our analyses, $\mathcal{R}_{\rm multi}$ for Type X with

$m_A = m_{H^\pm}$ has the largest value as 21% at $m_A - m_H \simeq -130$ GeV. It also gets its maximum value at $\tan\beta \simeq 2$ and $m_3 \simeq 0$. We have found that the region for multi-step PTs with $m_A - m_H \simeq -130$ GeV is realized for $\tan\beta \simeq 2$ in this case, so that such a region is excluded by the constraints from both $B \to \mu^+\mu^-$ and $H \to AZ$ [108]. In the region allowed by the $B \to \mu^+\mu^-$ constraint, we have also found that $\mathcal{R}_{\rm multi}$ has a larger value for $m_A - m_H < 0$, e.g. $\mathcal{R}_{\rm multi} = 9\%$ for $m_A - m_H \simeq -90$ GeV, and smaller $\tan\beta$.

On the other hand, strong two-step PTs only occur in the narrow region with $m_A > m_H$, as shown in the top right panel of Fig. 9. Moreover, the bottom right panel of Fig. 9 shows that strong two-step PTs happen only for $m_3 \lesssim 15$ GeV and they predict $\xi \simeq$1–1.3. Although the points for strong two-step PTs do not receive the constraint from $B \to \mu^+\mu^-$, those with $m_H \simeq 150$ GeV would be excluded by the $A \to HZ$ search [108], while those with $m_H \simeq 330$ GeV remain.

As above, the parameter region where multi-step PTs occur in this case becomes narrow compared with Type I 2HDMs with $m_A = m_{H^\pm}$. The Yukawa coupling of the top quark is same among the types, as in Table 1, and therefore the contribution of the top quark, which gives the fermion's largest contribution to $V_{\rm CW}$, is not dependent on the types. According to this, the reason for the narrow region in the analysis would be the difference of the range of $\cos(\beta - \alpha)$. As proof of that, we have confirmed that the result for $\cos(\beta - \alpha) = 0$ for Type I 2HDMs with $m_A = m_{H^\pm}$ has the same tendency as Type X 2HDMs with $m_A = m_{H^\pm}$.

5.2.2 *Type X* ($m_H = m_{H^\pm}$). Figure 10 shows the parameter points where one-step and multi-step PTs (left) and strong two-step PTs (right) occur in Type X 2HDMs with $m_H = m_{H^\pm}$ in the m_A vs. m_H (top), m_A vs. $\tan\beta$ (middle), and ξ vs. m_3 (bottom) planes. In this case we have found that there are no parameter points where more-than-three-step PTs occur, therefore the purple points show the points for only three-step PTs. Although the largest value of m_A for multi-step PTs is larger than for Type X with $m_A = m_{H^\pm}$, the other tendencies in Fig. 10 are similar. The maximum value of ξ for multi-step PTs reaches near 2 in the bottom left panel. We have found that $\mathcal{R}_{\rm multi}$ is largest at $m_A - m_H \simeq -210$ GeV, $\tan\beta \simeq 2$, and $m_3 \simeq 0$ (cf. Table B1 of Appendix B). However, the region with a large magnitude of negative $m_A - m_H$, which is found at $\tan\beta \simeq 2$, is excluded by the constraint from $H \to AZ$ decay [108]. On the other hand, in the region where the $H \to AZ$ channel does not open, we find that $\mathcal{R}_{\rm multi}$ is obtained for $m_A < m_H$ as, e.g., $\mathcal{R}_{\rm multi} = 5\%$ for $m_A - m_H \simeq -80$ GeV.

Meanwhile, from the top right panel in Fig. 10, as in the other cases, strong two-step PTs only occur when the mass hierarchy $m_A > m_H$ exists with $\tan\beta \simeq 2$. Additionally, they happen when m_3 is small, such as $m_3 \lesssim 30$ GeV in the bottom right panel of Fig. 10. The constraint from $B \to \mu^+\mu^-$ excludes the part of the region where multi-step PTs happen, e.g. 290 GeV $\lesssim m_H \lesssim$ 340 GeV, and hence the region for strong two-step PTs is excluded. We have confirmed that the result for $\cos(\beta - \alpha) = 0$ in Type I 2HDMs with $m_H = m_{H^\pm}$ has same tendency as for Type X 2HDMs with $m_H = m_{H^\pm}$.

To summarize briefly, the region where multi-step PTs are likely to occur is where $m_A - m_H$ is negative with a large magnitude, $\tan\beta$ is small, $\cos(\beta - \alpha)$ is negative and small for Type I 2HDMs (it is fixed at zero for Type X 2HDMs), and m_3 is small. Different from multi-step PTs, strong multi-step PTs occur only when the mass hierarchy $m_A > m_H$ exists, while the tendencies for the other parameters are similar. Finally, we show the results for two specific

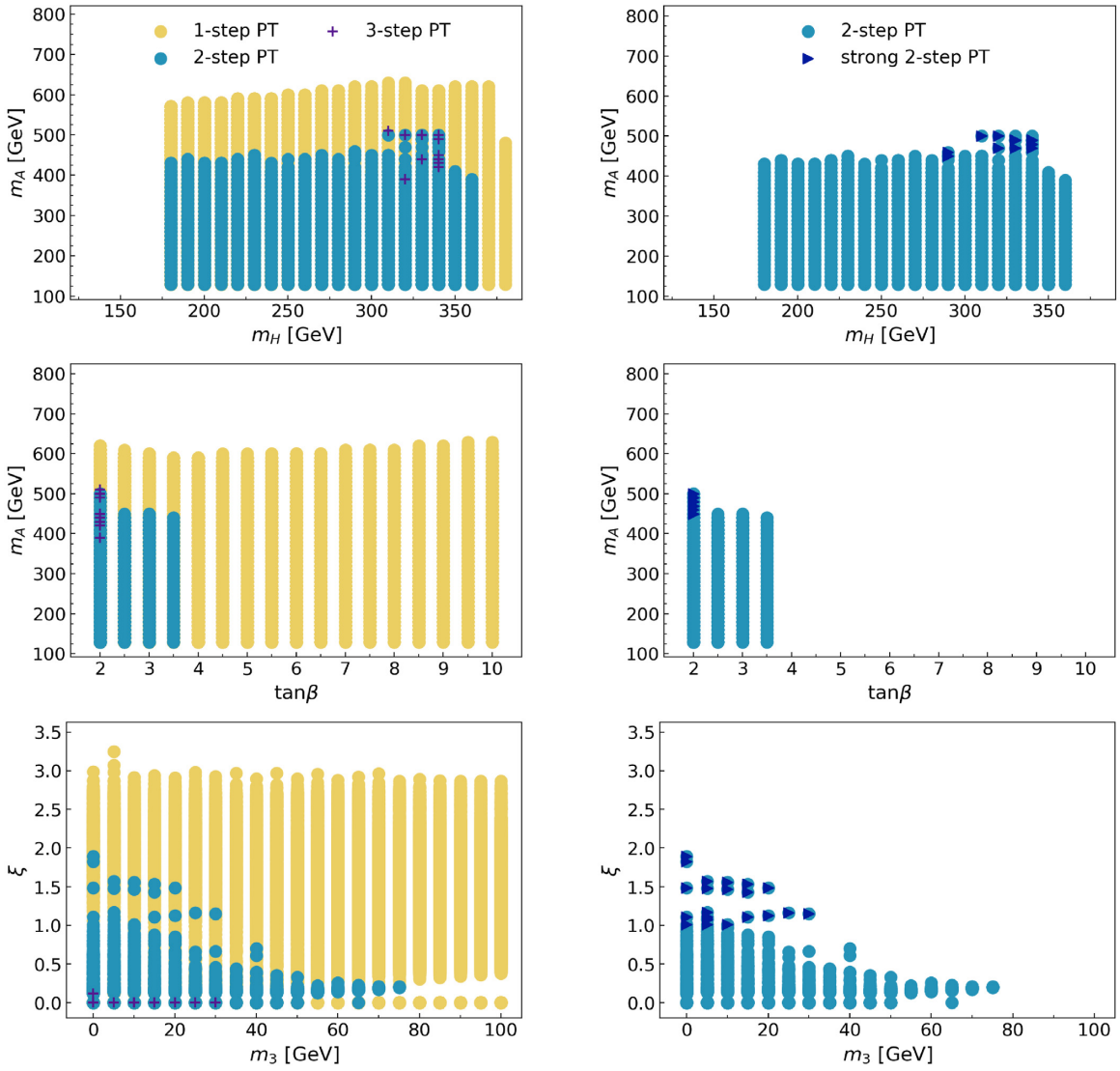

Fig. 10. As Fig. 9 but for Type X 2HDMs with $m_H = m_{H^\pm}$.

cases. Figure 11 shows the parameter points where the one-step, two-step, strong two-step, and three-or-more-step PTs occur in the m_A vs. m_H plane for Type I 2HDMs with $m_A = m_{H^\pm}$. The other input parameters are fixed as $\tan\beta = 2$, $\cos(\beta - \alpha) = -0.2$ (left panel) or 0 (right panel), and $m_3 = 0$. We can see that the regions for one-step and multi-step PTs are almost divided. In addition, $\mathcal{R}_{\rm multi}$ in the left panel of Fig. 11 is larger than in the right panel, which implies that multi-step PTs favor negative values of $\cos(\beta - \alpha)$. We also find that strong two-step PTs occur only with the mass hierarchy $m_A > m_H$. The above features are also seen for Type I 2HDMs with $m_H = m_{H^\pm}$. Note that the right panel of Fig. 11 has similar tendencies to the result for Type X 2HDMs with $m_A = m_{H^\pm}$ as described before. Taking into account the constraint from $B \to \mu\mu$ decays, the region of $m_A\ (= m_{H^\pm}) \lesssim 340\,\text{GeV}$ is excluded. In the survival parameter space in the left panel of Fig. 11, multi-step PTs occur most for $m_H \gtrsim 300\,\text{GeV}$. The region might be tested by the extra Higgs boson search of $A \to HZ$ if $m_A - m_H > m_Z$.

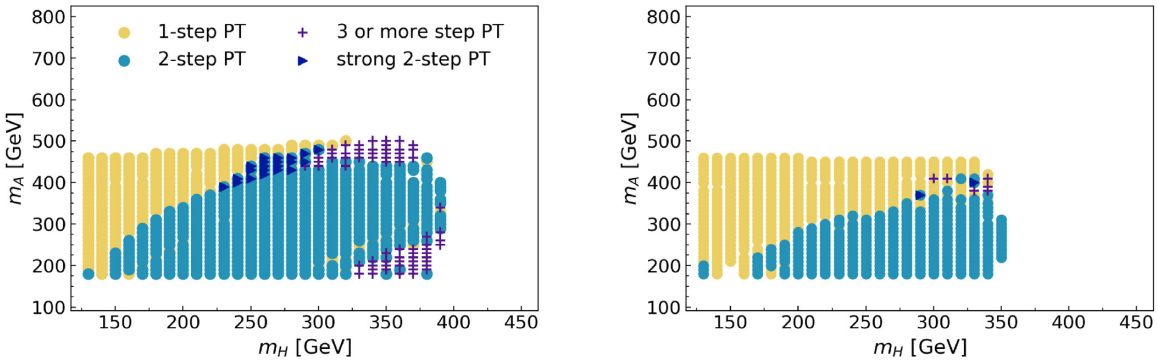

Fig. 11. Parameter points where the one-step, two-step, strong two-step, and three-or-more-step PTs occur in the m_A vs. m_H plane for Type I 2HDMs with $m_A = m_{H^\pm}$. The left (right) panel shows the results at $\tan\beta = 2$, $\cos(\beta - \alpha) = -0.2$ (0), and $m_3 = 0$.

6. Physical signatures

6.1 *Higgs trilinear couplings*

In this section, to research the possibility of verifying multi-step PTs by collider experiments, we discuss the Higgs trilinear coupling λ_{hhh}. This is derived by calculating the third derivative of the effective potential with respect to the SM-like Higgs fields at the EW vacuum as

$$\lambda_{hhh} = \left.\frac{\partial^3 V_{eff}^{T=0}(\phi_1, \phi_2)}{\partial h^3}\right|_{(\phi_1,\phi_2)=(v_1,v_2)}, \tag{39}$$

with $V_{eff}^{T=0} \equiv V_0 + V_{\rm CW} + V_{\rm CT}$. The trilinear coupling corrected by the leading one-loop contribution of the top quarks in the SM is written by

$$\lambda_{hhh}^{\rm SM} \simeq \frac{3m_h^2}{v}\left[1 - \frac{N_c}{3\pi^2}\frac{m_t^4}{v^2 m_h^2}\right], \tag{40}$$

where N_c is the color number of the top quarks. We determine the deviation of the Higgs trilinear coupling from that in the SM as

$$\delta\lambda_{hhh} \equiv \frac{\lambda_{hhh} - \lambda_{hhh}^{\rm SM}}{\lambda_{hhh}^{\rm SM}}. \tag{41}$$

When $\delta\lambda_{hhh}$ is equal to zero, the coupling has the same value as in the SM. In the following, we analyze $\delta\lambda_{hhh}$ with Type I and X 2HDMs.

The current limits on the Higgs trilinear coupling from Higgs pair production are $-4.2 < \delta\lambda_{hhh} < 10.9$ (at 95% CL) from ATLAS [109]. Future measurements, like the HL-LHC, could reach an accuracy of about 50%–60% with 3 ab^{-1} data [75], while the ILC operating at 500 GeV has the possibility of measuring $\delta\lambda_{hhh}$ with 27 % of precision [76].

6.1.1 *Type I* ($m_A = m_{H^\pm}$).

Figure 12 shows $\delta\lambda_{hhh}$ in the region where the one-step, two-step, and three-or-more-step PTs occur for Type I 2HDMs with $m_A = m_{H^\pm}$ as a function of m_A (upper left), $\tan\beta$ (upper right), and $\cos(\beta - \alpha)$ (lower left). In the upper left panel, the parameter points where multi-step PTs happen are located on the upper side of the plots in the region $m_A \gtrsim 300$ GeV. In other words, compared with the results for one-step PTs, the values of $\delta\lambda_{hhh}$ for multi-step PTs have a tendency to be large at the same value of m_A. The upper right panel shows that the smaller $\tan\beta$ is, the larger the maximum value of $\delta\lambda_{hhh}$ is for $\tan\beta \lesssim 8$. In the lower

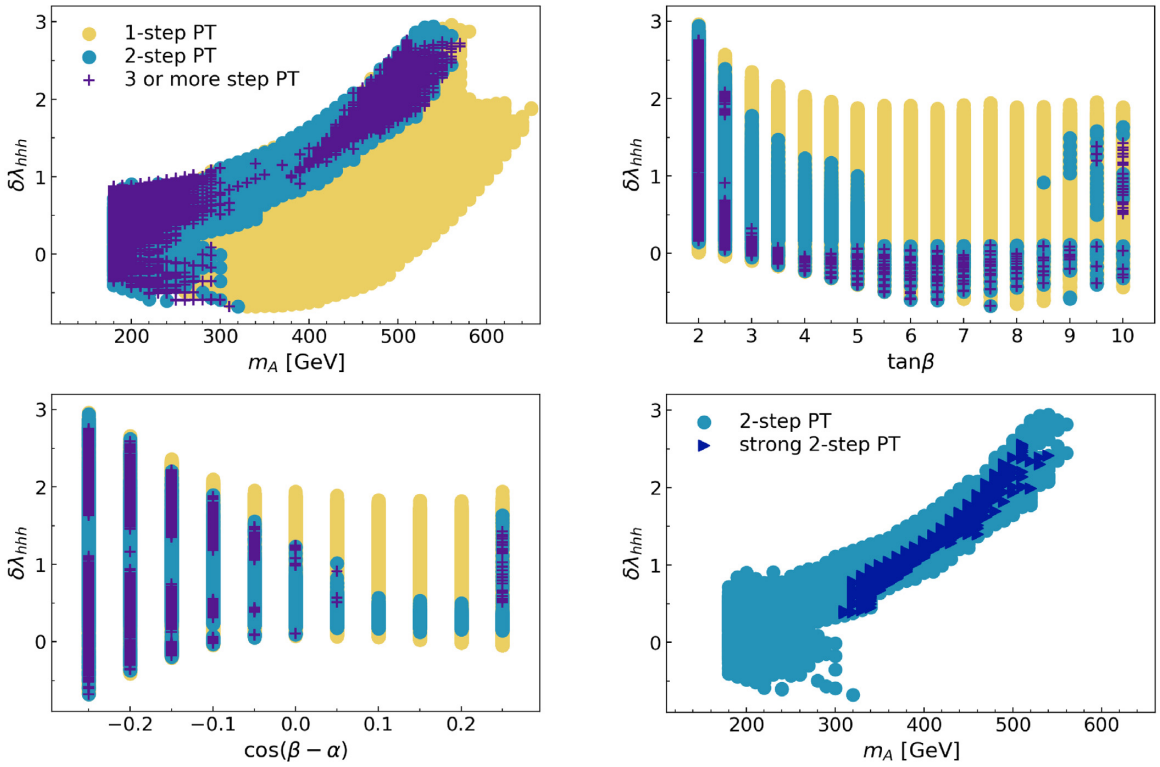

Fig. 12. Predictions for $\delta\lambda_{hhh}$ for Type I 2HDMs with $m_A = m_{H^\pm}$. The panels, except for the lower right, show $\delta\lambda_{hhh}$ where one-step, two-step, and three-or-more-step PTs occur for m_A (upper left), tan β (upper right), and cos $(\beta - \alpha)$ (lower left). The lower right plane shows $\delta\lambda_{hhh}$ where two-step and strong two-step PTs happen for m_A.

left panel, when multi-step PTs occur, the maximum value of $\delta\lambda_{hhh}$ becomes larger as cos $(\beta - \alpha)$ gets smaller, except for cos $(\beta - \alpha) \simeq 0.25$, especially for negative values of cos $(\beta - \alpha)$. Note that there are parameter points that have negative deviations. They are in $|\cos(\beta - \alpha)| \gtrsim 0.1$ and $m_3 \gtrsim 50$ GeV, as found by our analysis. The region where $\delta\lambda_{hhh} \simeq 2.5$ for multi-step PTs is 490 GeV $\lesssim m_A \lesssim$ 560 GeV, tan $\beta \simeq 2$, and cos $(\beta - \alpha) \lesssim -0.2$ in our parameter space. In this region we find that m_H is in 320 GeV $\lesssim m_H \lesssim$ 410 GeV.

The lower right panel of Fig. 12 shows $\delta\lambda_{hhh}$ for the two-step and strong two-step PTs as a function of m_A. It indicates that $\delta\lambda_{hhh}$ has the possibility of being as large as 0.5–2.5 when strong two-step PTs happen. When $\delta\lambda_{hhh}$ is 2.5 with a strong two-step PT, we found $m_A \simeq 510$ GeV, $m_H \simeq 320$ GeV, tan $\beta \simeq 2$, and cos $(\beta - \alpha) \simeq -0.25$. The deviations $\delta\lambda_{hhh} \simeq$0.5–2.5 would be tested at future colliders such as the HL-LHC and ILC.

6.1.2 *Type I* ($m_H = m_{H^\pm}$). The deviations $\delta\lambda_{hhh}$ for Type I 2HDMs with $m_H = m_{H^\pm}$ are shown in Fig. 13. In the upper left panel, the parameter points where multi-step PTs occur are located on the upper side, for $m_A \gtrsim 400$ GeV. The behavior of the predictions for multi-step PTs in Fig. 13 are similar to the Type I 2HDMs with $m_A = m_{H^\pm}$. From the panels except for the lower right panel in Fig. 13, we find that the region where multi-step PTs occur with $\delta\lambda_{hhh} \simeq 2.5$ is 590 GeV $\lesssim m_A \lesssim$ 640 GeV, tan $\beta \simeq 2$, and cos $(\beta - \alpha) \lesssim -0.2$. In this region, the range of m_H is 370 GeV $\lesssim m_H \lesssim$ 420 GeV. Additionally, in the lower right panel of Fig. 13, the range of $\delta\lambda_{hhh}$ for strong two-step PTs occuring is about 0.5–2.0, while the largest value of such $\delta\lambda_{hhh}$ is

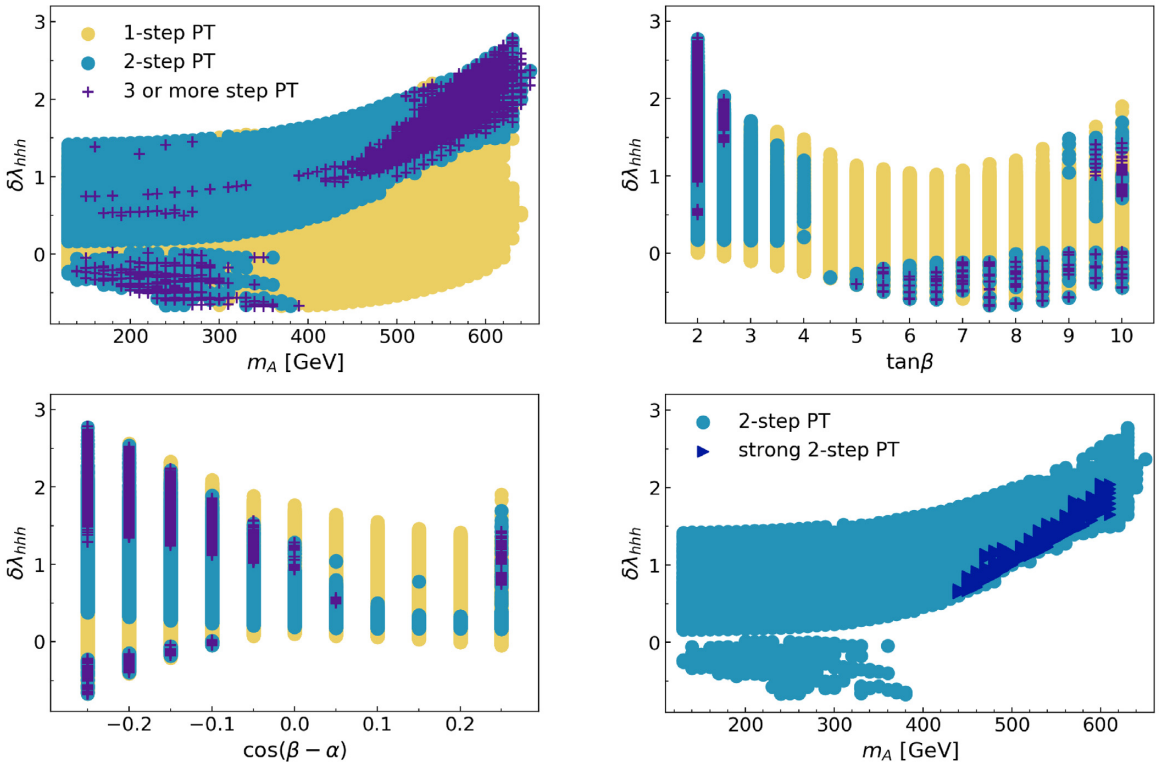

Fig. 13. As Fig. 12 but for Type I 2HDMs with $m_H = m_{H^\pm}$.

slightly smaller than for Type I 2HDMs with $m_A = m_{H^\pm}$. When $\delta\lambda_{hhh}$ is 2 with strong two-step PTs, we found 600 GeV $\lesssim m_A \lesssim$ 610 GeV, 300 GeV $\lesssim m_H \lesssim$ 360 GeV, $\tan\beta \simeq 2$, and $\cos(\beta - \alpha) \lesssim -0.15$. Although the constraint from $B \to \mu^+\mu^-$ excludes the part of the above region (especially the region with $m_H \simeq$ 330–340 GeV as described in Sect. 5.1.2), it still remains, and such $\delta\lambda_{hhh}$ could be tested at future collider experiments.

6.1.3 *Type X* ($m_A = m_{H^\pm}$). Figure 14 gives $\delta\lambda_{hhh}$ in the region where the one-step, two-step, and three-or-more-step PTs occur for Type X 2HDMs with $m_A = m_{H^\pm}$ as a function of m_A (upper left), $\tan\beta$ (upper right), and m_3 (lower left). We take $\cos(\beta - \alpha) = 0$ (alignment limit) in the Type X 2HDMs. In the upper left panel, the shape of the region where multi-step PTs occur is narrow, hence the value of $\delta\lambda_{hhh}$ is predictable when m_A is fixed. The largest value of $\delta\lambda_{hhh}$ for multi-step PTs is about 1.2 at $m_A \simeq$ 400 GeV, $\tan\beta \simeq 2$, and $m_3 \lesssim$ 20 GeV, and 310 GeV $\lesssim m_H \lesssim$ 340 GeV. Although the largest value is smaller than for Type I 2HDMs, it can be accessed at future collider experiments. The lower left panel shows that the values of $\delta\lambda_{hhh}$ for multi-step PTs converge to around 0.7 as m_3 gets larger. Such dependence of $\delta\lambda_{hhh}$ on m_3 is not seen for Type I 2HDMs. Moreover, the predicted values of $\delta\lambda_{hhh}$ stay positive in all regions, although negative $\delta\lambda_{hhh}$ are also predicted for Type I 2HDMs. These differences between Type I and Type X are mainly due to the range of $\cos(\beta - \alpha)$. The lower right panel in Fig. 14 shows that the range where strong two-step PTs occur is $0.5 \lesssim \delta\lambda_{hhh} \lesssim 1.2$. When $\delta\lambda_{hhh}$ is 1.2 with strong two-step PTs, we found $m_A \simeq$ 400 GeV, $m_H \simeq$ 340 GeV, and $\tan\beta \simeq 2$. The deviations $\delta\lambda_{hhh} \simeq$ 0.5–1.2 could be explored at future colliders like the HL-LHC and ILC.

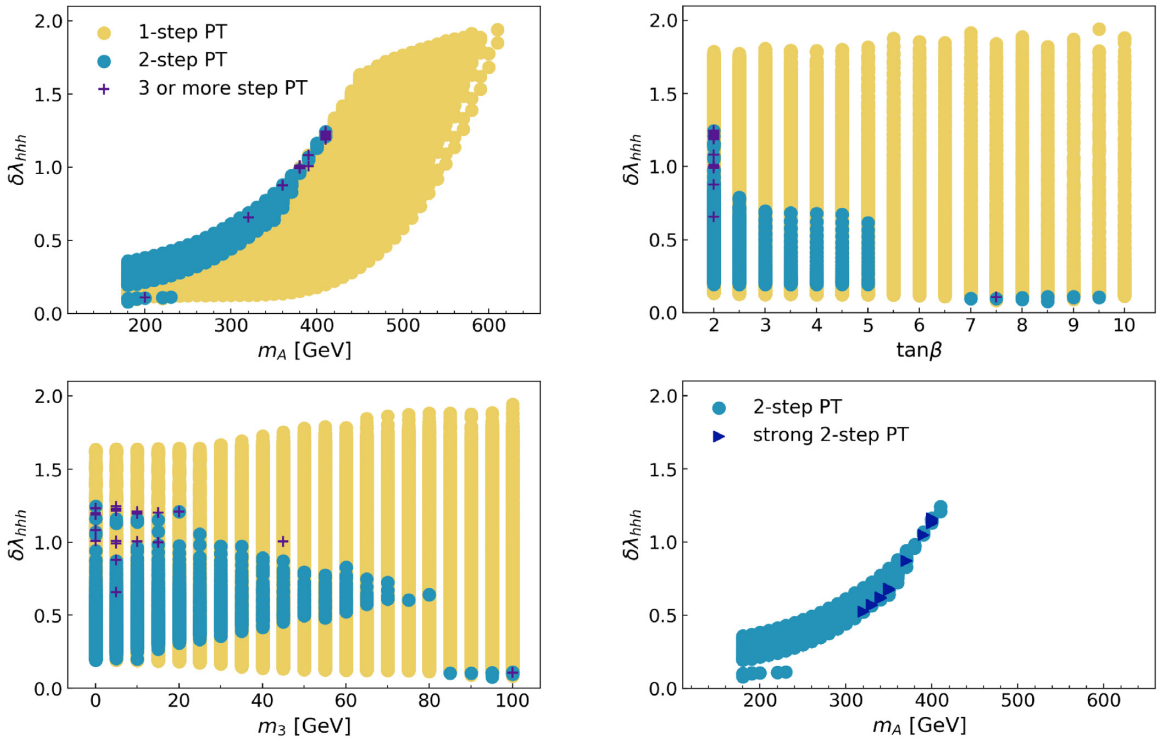

Fig. 14. Predictions for $\delta\lambda_{hhh}$ for Type I 2HDMs with $m_A = m_{H^\pm}$. The panels except for the lower right panel show $\delta\lambda_{hhh}$ where the one-step, two-step, and three-or-more-step PTs occur for m_A (upper left), $\tan\beta$ (upper right), and m_3 (lower left). The lower right plane shows $\delta\lambda_{hhh}$ where two-step and strong two-step PTs happen for m_A.

6.1.4 *Type X* ($m_H = m_{H^\pm}$). The deviations $\delta\lambda_{hhh}$ for Type X 2HDMs with $m_H = m_{H^\pm}$ are shown in Fig. 15. We obtain similar features to the Type X 2HDMs with $m_A = m_{H^\pm}$, except that the region where multi-step PTs occur gets broader upward. From Fig. 15 except for the lower right panel (also from the top left panel in Fig. 10), we see that $\delta\lambda_{hhh} \simeq 1.2$ for multi-step PTs is predicted for 480 GeV $\lesssim m_A \lesssim$ 510 GeV, $\tan\beta \simeq 2$, $m_3 \lesssim 30$ GeV, and 310 GeV $\lesssim m_H \lesssim$ 340 GeV. However, this region is excluded by the constraint from $B \to \mu^+\mu^-$ as described in Sect. 5.2.2. Nevertheless, when $m_A \simeq 400$ GeV, the maximum value of $\delta\lambda_{hhh} \simeq 0.9$ is allowed by the constraint, where the other parameters are $\tan\beta \simeq 2$, $m_3 \lesssim 40$ GeV, and $m_H \simeq 350$ GeV. Such a value of $\delta\lambda_{hhh}$ can be tested at future collider experiments. In the lower right panel in Fig. 15, we see that strong two-step PTs give $\delta\lambda_{hhh} \simeq 1.2$ around $m_A \simeq 490$ GeV. However, all the regions where strong two-step PTs occur are excluded by the constraint from $B \to \mu^+\mu^-$, as mentioned in Sect. 5.2.2.

Figure 16 shows the predictions for $\delta\lambda_{hhh}$ in the two cases in Fig. 11. In the left (right) panel of Fig. 16, we take $\tan\beta = 2$, $\cos(\beta - \alpha) = -0.2$ (0), and $m_3 = 0$ for Type I 2HDMs with $m_A = m_{H^\pm}$. Compared with the same value of m_A, $\delta\lambda_{hhh}$ for multi-step PTs has the tendency to be larger than for one-step PTs. We can also see the largest value of $\delta\lambda_{hhh}$ where multi-step PTs occur at $\cos(\beta - \alpha) = -0.2$ (left) is greater than at $\cos(\beta - \alpha) = 0$ (right). Meanwhile, $\delta\lambda_{hhh}$ for strong two-step PTs is relatively large at about $\delta\lambda_{hhh} \simeq$ 1–2 (left) and $\simeq 1$ (right), respectively. The regions for the strong two-step PTs do not receive the constraint from $B \to \mu\mu$ decays since m_A ($= m_{H^\pm}$) > 340 GeV.

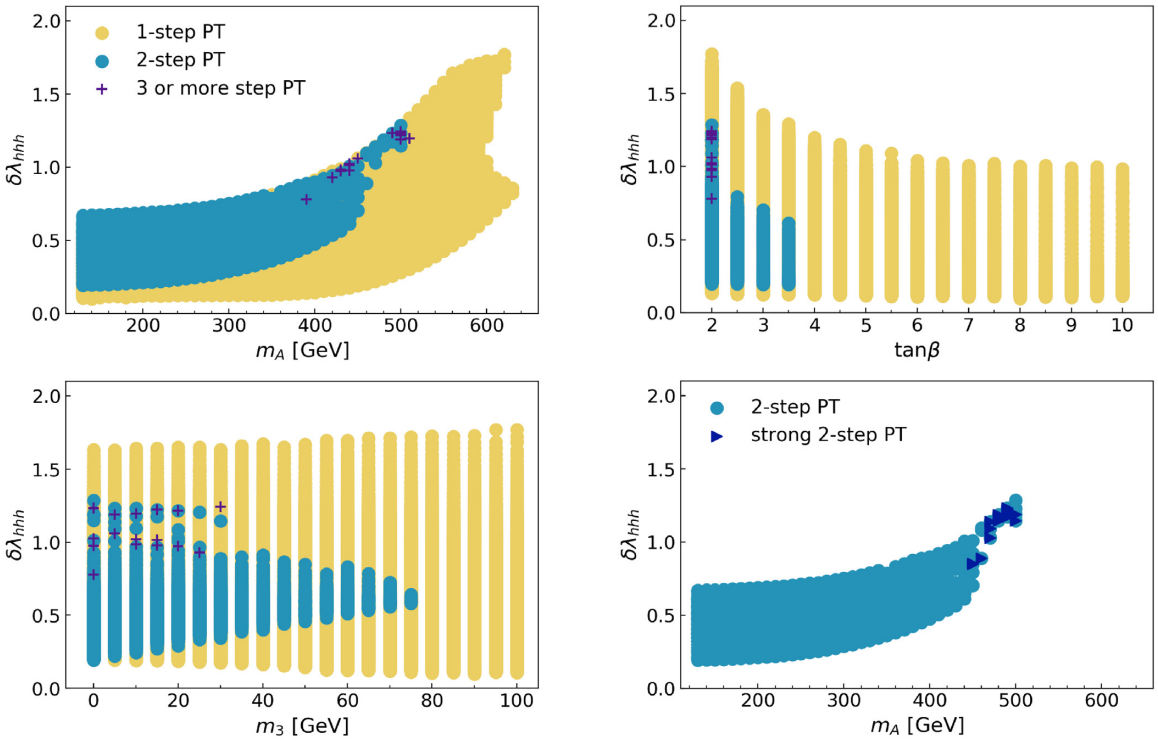

Fig. 15. As Fig. 14 but for Type X 2HDMs with $m_H = m_{H^\pm}$.

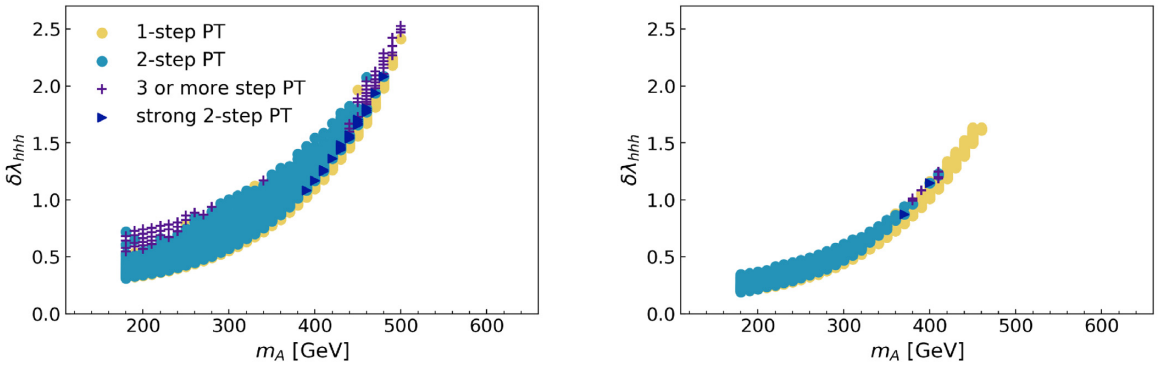

Fig. 16. Predictions for $\delta\lambda_{hhh}$ where the one-step, two-step, strong two-step, and three-or-more-step PTs occur for m_A in Type I 2HDMs with $m_A = m_{H^\pm}$. The left (right) panel shows $\delta\lambda_{hhh}$ at $\tan\beta = 2$, $\cos(\beta - \alpha) = -0.2$ (0), and $m_3 = 0$.

6.2 *Gravitational waves from multi-step PT*

The first-order PT at the EW scale is a source of GWs whose typical spectrum has a peak frequency. Therefore, if a first-order PT occurs multiple times in a multi-step EWPT, multi-peaked GWs can be observed in space-based interferometers. In this subsection we study such a possibility in the case of two-step PTs.

The GW spectrum is characterized by two parameters, $\alpha_{\rm GW}$ and $\tilde{\beta}_{\rm GW}$, at the nuclear temperature T_n. Here, T_n is determined by the condition that one bubble nucleates per Hubble radius, $S_3/T_n \simeq 140$, where S_3 is the O(3) symmetric action. $\alpha_{\rm GW}$ is given by

$$\alpha_{\rm GW} \equiv \frac{\epsilon(T_n)}{\rho_{\rm rad}(T_n)}, \tag{42}$$

which is the ratio of the latent heat $\epsilon(T_n)$ to the radiation density $\rho_{\rm rad}(T_n) = g_*(\pi^2 T_n^4)/30$, where g_* is 110.75 in 2HDMs. The latent heat in the first-order PT is calculated as

$$\epsilon(T_n) = \left[-\Delta V + T\frac{\partial \Delta V}{\partial T}\right]\Big|_{T=T_n}, \tag{43}$$

where ΔV is the difference between the effective potentials of the two phases before and after the PT. On the other hand, $\tilde{\beta}_{\rm GW}$ is defined as $\tilde{\beta}_{\rm GW} \equiv \beta_{\rm GW}/H_n$, where H_n is the Hubble parameter at T_n and $\beta_{\rm GW}$ is the inverse time duration of the PT,

$$\beta_{\rm GW} \equiv H_n T_n \frac{d}{dT}\left(\frac{S_3(T)}{T}\right)\Big|_{T=T_n}. \tag{44}$$

There are three contributions to the GW spectrum at a first-order PT:

$$h^2\Omega_{\rm GW}(f) = h^2\Omega_\varphi(f) + h^2\Omega_{\rm sw}(f) + h^2\Omega_{\rm turb}(f). \tag{45}$$

Here, h is the dimensionless Hubble parameter, f is the frequency of the GW at present, Ω_φ is the scalar field contribution from collisions of bubble walls [110–115], $\Omega_{\rm sw}$ is the contribution from sound waves surrounding the bubble walls [116–119], and $\Omega_{\rm turb}$ is the contribution from magnetohydrodynamic (MHD) turbulence in the plasma [120–125]. Each contribution is given by $\alpha_{\rm GW}$ and $\tilde{\beta}_{\rm GW}$ with the velocity of the bubble wall $v_{\rm w}$ and κ_φ, $\kappa_{\rm sw}$, and $\kappa_{\rm turb}$, which are the fractions of vacuum energy respectively converted into the gradient energy of the scalar field, the bulk motion of the fluid, and MHD turbulence. Numerical simulations and analytic estimates of the individual contributions lead to the following formulas:

scalar field contribution Ω_φ [115]:

$$h^2\,\Omega_\varphi(f) = 1.67\times10^{-5}\tilde{\beta}_{\rm GW}^{-2}\left(\frac{\kappa_\varphi\alpha_{\rm GW}}{1+\alpha_{\rm GW}}\right)^2\left(\frac{100}{g_*}\right)^{1/3}\left(\frac{0.11v_{\rm w}^3}{0.42+v_{\rm w}^2}\right)\frac{3.8(f/f_\varphi)^{2.8}}{1+2.8(f/f_\varphi)^{3.8}}, \tag{46}$$

where the peak frequency is

$$f_\varphi = 16.5\times10^{-6}\tilde{\beta}_{\rm GW}\left(\frac{0.62}{1.8-0.1v_{\rm w}+v_{\rm w}^2}\right)\left(\frac{T_n}{100\,{\rm GeV}}\right)\left(\frac{g_*}{100}\right)^{1/6}{\rm Hz}; \tag{47}$$

sound-wave contribution $\Omega_{\rm sw}$ [119]:

$$h^2\,\Omega_{\rm sw}(f) = 2.65\times10^{-6}\tilde{\beta}_{\rm GW}^{-1}\left(\frac{\kappa_{\rm sw}\alpha_{\rm GW}}{1+\alpha_{\rm GW}}\right)^2\left(\frac{100}{g_*}\right)^{1/3}v_{\rm w}(f/f_{\rm sw})^3\left(\frac{7}{4+3(f/f_{\rm sw})^2}\right)^{7/2}, \tag{48}$$

where the peak frequency is

$$f_{\rm sw} = 1.9\times10^{-5}v_{\rm w}^{-1}\tilde{\beta}_{\rm GW}\left(\frac{T_n}{100\,{\rm GeV}}\right)\left(\frac{g_*}{100}\right)^{1/6}{\rm Hz}; \tag{49}$$

MHD turbulence contribution $\Omega_{\rm turb}$ [124,125]:

$$h^2\,\Omega_{\rm turb}(f) = 3.35\times10^{-4}\tilde{\beta}_{\rm GW}^{-1}\left(\frac{\kappa_{\rm turb}\alpha_{\rm GW}}{1+\alpha_{\rm GW}}\right)^{\frac{3}{2}}\left(\frac{100}{g_*}\right)^{1/3}v_{\rm w}\frac{(f/f_{\rm turb})^3}{[1+(f/f_{\rm turb})]^{\frac{11}{3}}(1+8\pi f/h_n)}, \tag{50}$$

where the peak frequency is

$$f_{\rm turb} = 2.7\times10^{-5}v_{\rm w}^{-1}\tilde{\beta}_{\rm GW}\left(\frac{T_n}{100\,{\rm GeV}}\right)\left(\frac{g_*}{100}\right)^{1/6}{\rm Hz}, \tag{51}$$

and

$$h_n = 1.65\times10^{-5}\left(\frac{T_n}{100\,{\rm GeV}}\right)\left(\frac{g_*}{100}\right)^{1/6}{\rm Hz}. \tag{52}$$

We assume the bubble wall velocity to be $v_{\rm w} = 1$ for simplicity, and set [113,126]

$$\kappa_\varphi \simeq \frac{1}{1+0.715\alpha_{\rm GW}}\left(0.715\alpha_{\rm GW} + \frac{4}{27}\sqrt{\frac{3\alpha_{\rm GW}}{2}}\right), \tag{53}$$

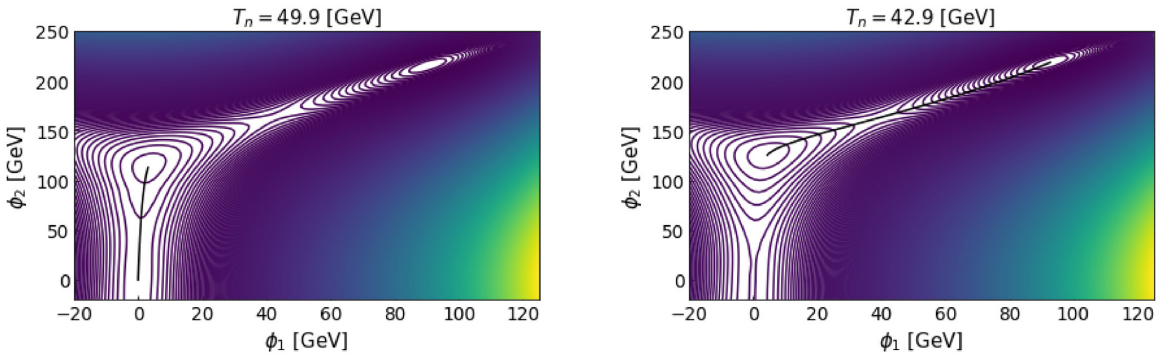

Fig. 17. Left (Right): Contour plots of the effective potential and the path of the first- (second-) step PT at $T_n = 49.9$ (42.9) GeV for the benchmark point.

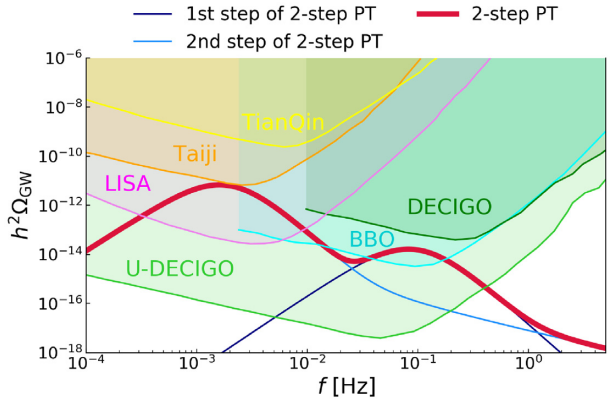

Fig. 18. GW spectrums from the first and second steps of strong two-step PTs for the benchmark point. The navy and blue lines represent the GW spectrums from the first- and second-step PTs, respectively. The red line shows the superposed GW spectrum.

$$\kappa_{\rm sw} \simeq \frac{\alpha}{0.73+0.083\sqrt{\alpha_{\rm GW}}+\alpha_{\rm GW}}, \tag{54}$$

and $\kappa_{\rm turb} \approx 0.1\kappa_{\rm sw}$ [119].

We compute the GW spectrums from a strong two-step PT where both the first- and second-step PTs are first order. The following parameter set for a Type I 2HDM is chosen as a benchmark point: $m_A = m_{H^\pm} = 490\,\text{GeV}$, $m_H = 300\,\text{GeV}$, $\tan\beta = 2.3$, $\cos(\beta-\alpha) = -0.21$, $m_3 = 20\,\text{GeV}$. In the left and right panels of Fig. 17, the paths of the first and second PTs in a strong two-step PT are shown by black lines in the ϕ_2 vs. ϕ_1 plane. Contour plots of the effective potential at T_n are also given in Fig. 17. The path of the first-step PT runs almost along the ϕ_2 axis from the origin to $(\phi_1, \phi_2) \simeq (3\,\text{GeV}, 115\,\text{GeV})$ at $T_n \simeq 49.9\,\text{GeV}$. The path of the second-step PT goes from $(\phi_1, \phi_2) \simeq (5\,\text{GeV}, 126\,\text{GeV})$ to $(\phi_1, \phi_2) \simeq (93\,\text{GeV}, 219\,\text{GeV})$, which is in the direction of the EW vacuum, at $T_n = 42.9\,\text{GeV}$. The strengths of the first- and second-step PTs are respectively $\xi = 2.1$ and 4.2, so both of them satisfy the criterion $\xi \geq 1$. The values of $(\alpha_{\rm GW}, \tilde{\beta}_{\rm GW})$ are $(8.1\times10^{-2}, 8.5\times10^{3})$ for the first step and $(0.16, 1.9\times10^{2})$ for the second step. The GW spectrums $h^2\,\Omega_{\rm GW}$ from these PTs are shown in Fig. 18. The areas observable by future space-based interferometers such as LISA [30–32], DECIGO [127, 128], BBO [77], U-DECIGO [78], Taiji [129, 130], and TianQin [131, 132] are also presented. The navy and blue lines represent the GW spectrums from the first- and second-step PTs, which

have peak frequencies around 0.1 Hz and 2×10^{-3} Hz, respectively. The superposed GW spectrum is shown by the red line. We can see that it has a double peak, which can be observed by BBO or U-DECIGO.[11] Additionally, the deviation of the Higgs trilinear coupling $\delta\lambda_{hhh}$ is 2.2 for the benchmark point. Such a $\delta\lambda_{hhh}$ has the possibility of being measured at the HL-LHC and ILC. Therefore, the signature of strong two-step PTs at the benchmark point may be observed in both GW and collider experiments. With a combination of these signatures, it might be possible to identify whether strong two-step PTs occurred in the early universe.

7. Conclusions

We have studied the parameter regions where multi-step and strong two-step EWPTs occur by scanning the parameter spaces in CP-conserving Type I and Type X 2HDMs with m_A or $m_H = m_{H^\pm}$. In the analyses, we have focused on small m_3, $0 \leq m_3 \leq 100\,\text{GeV}$. As a result of our scan, areas where multi-step and strong two-step PTs occur have been found. The features of the parameter region where multi-step PTs are likely to occur are: (i) $m_A - m_H$ is negative with large magnitude, (ii) $\tan\beta$ is small, (iii) $\cos(\beta - \alpha)$ is negative and small, (iv) m_3 is small. Features (ii), (iii), and (iv) are preferred for negative m_2^2 with large magnitude, which can yield a minimum point along the ϕ_2 axis. By contrast, strong two-step PTs occur only when the mass hierarchy $m_A > m_H$ exists in our parameter search, while they have similar features to (ii), (iii), and (iv). On the other hand, the VEVs after the first step of multi-step PTs have a tendency to be located along the ϕ_2 (or ϕ_1) axis, and the VEVs after the last-step PTs are likely to lie in the direction of the EW vacuum.

As the possible physical signatures for multi-step PTs in collider experiments, we have investigated the deviation of the Higgs trilinear coupling $\delta\lambda_{hhh}$ from that in the SM. The maximum value of $\delta\lambda_{hhh}$ increases as $\tan\beta$ and $\cos(\beta - \alpha)$ (which is zero in Type X 2HDMs) become smaller in the case where multi-step PTs occur. Compared with the results for one-step PTs at the same value of m_A, the values of $\delta\lambda_{hhh}$ for multi-step PTs have a tendency to be large. In particular, when strong two-step PTs happen, $\delta\lambda_{hhh}$ is larger than about 0.5, and the largest value of $\delta\lambda_{hhh}$ in Type I 2HDMs reaches over 2. Such deviations could be measured at future colliders like the HL-LHC and ILC. As the signatures observed by the space-based interferometers, we have computed the GW spectrums from strong two-step PTs where the first-order PT occurs twice. The superposed GW spectrum has the possibility of a double peak and could be observed by future observers such as BBO and U-DECIGO. Multi-step EWPT might be confirmed by combining the information obtained from future collider and GW experiments.

Acknowledgments

The work of M. A. is supported in part by the Japan Society for the Promotion of Sciences Grants-in-Aid for Scientific Research (Grant Nos. 17K05412 and 20H00160).

Funding

Open Access funding: SCOAP[3].

[11] Recent studies in Ref. [133] suggest the existence of an additional suppression factor for Ω_{sw} due to the finite lifetime of the sound waves. The factors are about 0.005 and 0.1, respectively, for the first- and second-step PTs at our benchmark point. Taking into account the suppressions, the peak of the GW spectrum of the first-step PT can hardly be seen. However, there are still several uncertainties in the calculation of the GW spectrum (see Refs. [134–143] for recent work).

Appendix A. Complex effective potential at finite temperature

In this appendix we comment on the region where the complex effective potential appears at finite temperature. Figure A1 shows parameter points where two-step PTs occur for negative scalar squared masses at the origin for first-step PTs (light blue) in Type I 2HDMs with $m_A = m_{H^\pm}$. The scalar squared mass m_s^2 indicates the smallest squared mass among the scalar fields. The parameter points for two-step PTs (blue) are the same as in Fig. 4. The light-blue points almost overlap with the two-step PT points except for $\cos(\beta - \alpha) \simeq -0.05$–$0.15$.

Although the light-blue points are widespread in the parameter space, the ratio of the number of points for negative squared masses to that for all points where two-step PTs occur is about 15%. On the other hand, we also find that the parameter points for one-step PTs are also widespread, and the number ratio is about 25%. Reference [144] shows that the resummation method can cure the contributions from negative squared masses.

Appendix B. Tables for numerical analyses

We show in Tables B1 and B2 the values or ranges of input parameters where the ratios $\mathcal{R}_{\rm multi}$, Eq. (36), and $\mathcal{R}_{\rm st2}$, Eq. (37), have maximum values for Type I and X 2HDMs. Note that we omit the results for Type X 2HDMs in Table B2 because the number of points for strong two-step PTs in this case is not sufficient to consider the dependencies of the ratios on the input parameters. We see that, e.g., in Table B1 multi-step PTs favor $m_A < m_H$ in all four cases. Similar tendencies in Tables B1 and B2 are seen even if we consider the constraint from $B \to \mu^+\mu^-$.Although we do not discuss strong one-step PTs in Sect. 5, we also show the results of the numerical analyses for them here because they are still important in the context of baryogenesis. Figure A2 gives the number of points for one-step (yellow) and strong one-step (orange) PTs as functions of m_A (top), m_H (middle), and $m_A - m_H$ (bottom) for Type I 2HDMs with $m_A = m_{H^\pm}$. The red dashed lines represent $\mathcal{R}_{\rm st1}$, which are the ratios of the number of points for strong one-step PTs to that for one-step PTs,

$$\mathcal{R}_{\rm st1} = \frac{\#\text{ of points for strong onestep PTs}}{\#\text{ of points for onestep PTs}}. \tag{B1}$$

We see in the middle left panel that $\mathcal{R}_{\rm st1}$ peaks at $m_A - m_H \simeq 220\,\text{GeV}$ and reaches close to 1. Hence, strong one-step PTs favor the mass hierarchy $m_A > m_H$ (This is consistent with the

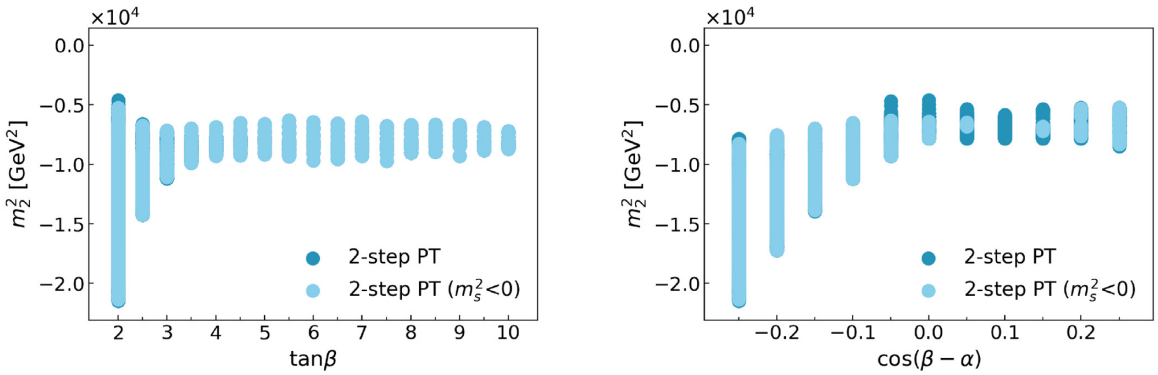

Fig. A1. Parameter points where two-step PTs (blue) and those with $m_s^2 < 0$ at the origin for the first-step PTs (light-blue) occur in the m_2^2 vs. $\tan\beta$ (left) and m_2^2 vs. $\cos(\beta - \alpha)$ (right) planes in Type I 2HDMs with $m_A = m_{H^\pm}$.

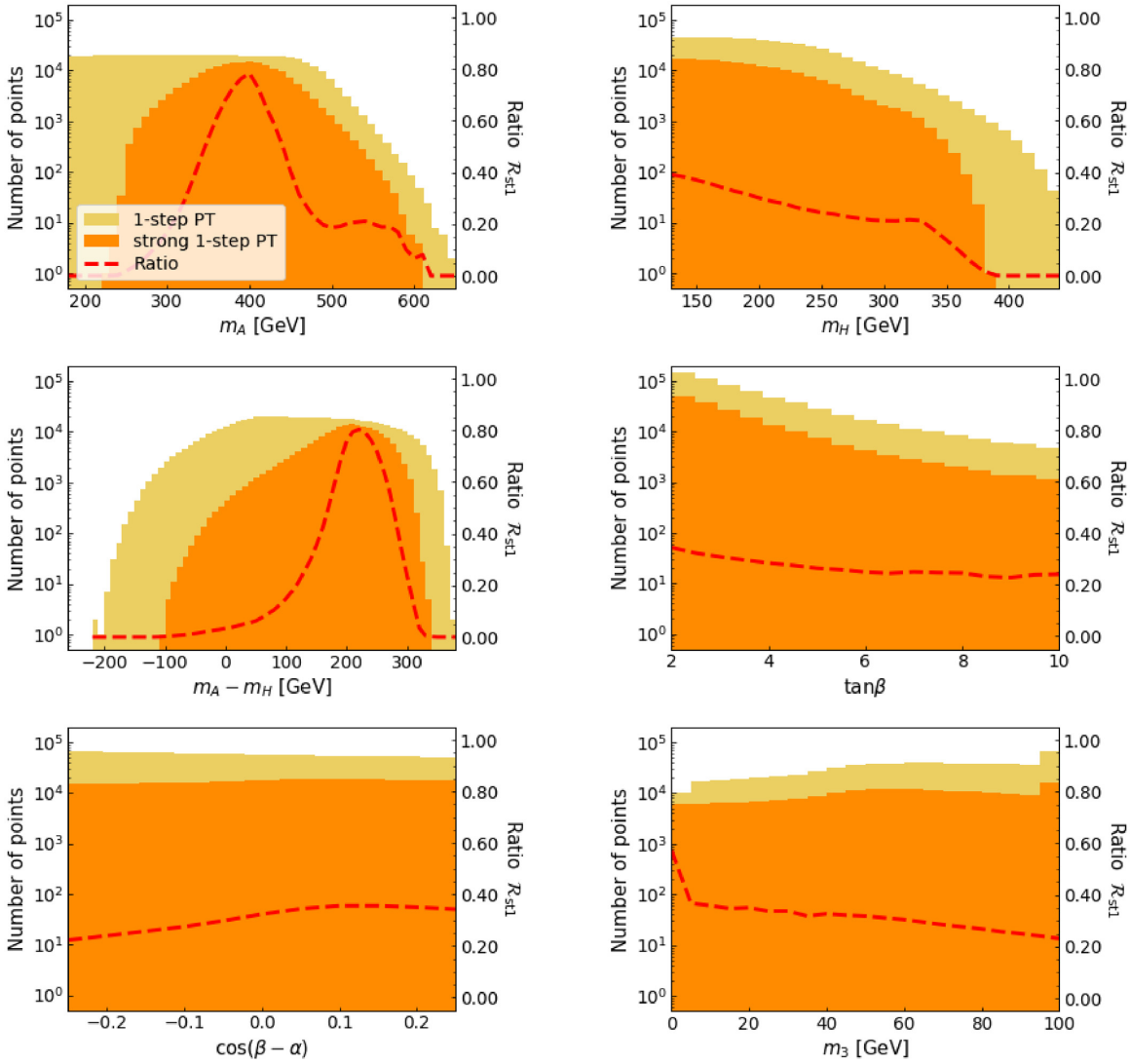

Fig. A2. Number of points where one-step (yellow) and strong one-step (orange) PTs occur as functions of m_A, m_H, $m_A - m_H$, $\tan\beta$, $\cos(\beta - \alpha)$, and m_3 in Type I 2HDMs with $m_A = m_{H^\pm}$. The red dashed line represents $R_{\rm st1}$, the ratio of the number of points where strong one-step PTs occur to that for one-step PTs.

Table B1. Values or ranges of input parameters where $\mathcal{R}_{\rm multi}$ takes maximum values. The values in parentheses represent the maximum values of $\mathcal{R}_{\rm multi}$.

	m_A [GeV]	m_H [GeV]	$m_A - m_H$ [GeV]	$\tan\beta$	$\cos(\beta - \alpha)$	m_3 [GeV]
Type I ($m_A = m_{H^\pm}$)	130–550 ($\sim$ 7%)	390 (47%)	−250 (100%)	2 (11%)	−0.25 (9%)	0 (48%)
Type I ($m_H = m_{H^\pm}$)	650 (100%)	360 (35%)	−210 (21%)	2 (13%)	−0.25 (9%)	0 (60%)
Type X ($m_A = m_{H^\pm}$)	310 (11%)	350 (36%)	−130 (21%)	2 (13%)	—	0 (49%)
Type X ($m_H = m_{H^\pm}$)	130–350 ($\sim$ 14%)	350 (38%)	−210 (50%)	2 (18%)	—	0 (60%)

Table B2. Values of input parameters where $\mathcal{R}_{\rm st2}$ takes maximum values. The values in parentheses represent the maximum values of $\mathcal{R}_{\rm st2}$. Note that we omit the results for Type X 2HDMs because the number of points for strong two-step PTs in these cases is not sufficient to consider the dependencies of the ratios on the input parameters.

	m_A [GeV]	m_H [GeV]	$m_A - m_H$ [GeV]	$\tan\beta$	$\cos(\beta-\alpha)$	m_3 [GeV]
Type I ($m_A = m_{H^\pm}$)	470 (41%)	280 (12%)	210 (100%)	2.5–4.5 ($\sim$ 10%)	−0.25 (11%)	20 (7%)
Type I ($m_H = m_{H^\pm}$)	580 (50%)	280 (8%)	310 (100%)	2.5–4 ($\sim$ 11%)	−0.25 (9%)	10 (5%)

Table B3. Values or ranges of input parameters where $\mathcal{R}_{\rm st1}$ takes maximum values. The values in parentheses represent the maximum values of $\mathcal{R}_{\rm st1}$.

	m_A [GeV]	m_H [GeV]	$m_A - m_H$ [GeV]	$\tan\beta$	$\cos(\beta-\alpha)$	m_3 [GeV]
Type I ($m_A = m_{H^\pm}$)	400 (78%)	130 (39%)	220 (80%)	2 (34%)	0.05–0.25 ($\sim$ 36%)	0 (57%)
Type I ($m_H = m_{H^\pm}$)	530 (83%)	130–340 (33%)	340 (91%)	2 (35%)	0.05–0.25 ($\sim$ 38%)	0 (66%)
Type X ($m_A = m_{H^\pm}$)	400 (91%)	130 (39%)	210 (83%)	2 (40%)	—	0 (59%)
Type X ($m_H = m_{H^\pm}$)	630 (100%)	360 (43%)	300 (85%)	2 (41%)	—	0 (64%)

results in Ref. [14].) This is the same feature as for strong two-step PTs, shown in the top right panel of Fig. 3.

We show in Table B3 the values or ranges of input parameters where the ratio $\mathcal{R}_{\rm st1}$, Eq. (B1), takes maximum values for Type I and X 2HDMs. Similar tendencies to Tables B1, B2, and B3 are seen even if we consider the constraint from $B \to \mu^+\mu^-$.

References

[1] N. Aghanim et al., Astron. Astrophys. **641**, A6 (2020).
[2] A. D. Sakharov, Sov. Phys. Usp. **34**, 392 (1991).
[3] V. A. Kuzmin, V. A. Rubakov, and M. E. Shaposhnikov, Phys. Lett. B **155**, 36 (1985).
[4] K. Kajantie, M. Laine, K. Rummukainen, and M. E. Shaposhnikov, Nucl. Phys. B **466**, 189 (1996).
[5] F. Csikor, Z. Fodor, and J. Heitger, Phys. Rev. Lett. **82**, 21 (1999).
[6] G. Aad et al., Phys. Lett. B **716**, 1 (2012).
[7] ATLAS Collaboration, Tech. Rep. ATLAS-CONF-2012-162, CERN, Geneva. (2012), http://cds.cern.ch/record/1494183.
[8] S. Chatrchyan et al., Phys. Lett. B **716**, 30 (2012).
[9] CMS Collaboration, Tech. Rep. CMS-PAS-HIG-12-045,CERN, Geneva. (2012), http://cds.cern.ch/record/1494149.
[10] M. D'Onofrio, K. Rummukainen, and A. Tranberg, Phys. Rev. Lett. **113**, 141602 (2014).
[11] M. B. Gavela, P. Hernandez, J. Orloff, and O. Pene, Mod. Phys. Lett. A **9**, 795 (1994).
[12] P. Huet and E. Sather, Phys. Rev. D **51**, 379 (1995).
[13] M. B. Gavela, P. Hernandez, J. Orloff, O. Pene, and C. Quimbay, Nucl. Phys. B **430**, 382 (1994).
[14] G. C. Dorsch, S. J. Huber, and J. M. No, J. High Energy Phys. **10**, 029 (2013).
[15] P. Basler, M. Krause, M. Muhlleitner, J. Wittbrodt, and A. Wlotzka, J. High Energy Phys., **02**, 121 (2017).
[16] J. Bernon, L. Bian, and Y. Jiang, J. High Energy Phys. **05**, 151 (2018).
[17] L. Wang, J. M. Yang, M. Zhang, and Y. Zhang, Phys. Lett. B **788**, 519 (2019).
[18] W. Su, A. G. Williams, and M. Zhang, J. High Energy Phys. **04**, 219 (2021).
[19] J. O. Andersen, T. Gorda, A. Helset, L. Niemi, T. V. I. Tenkanen, A. Tranberg, A. Vuorinen, and D. J. J. Weir, Phys. Rev. Lett. **121**, 191802 (2018).

[20] K. Kainulainen, V. Keus, L. Niemi, K. Rummukainen, T. V. I. Tenkanen, and V. Vaskonen, J. High Energy Phys. **06**, 075 (2019).
[21] A. Haarr, A. Kvellestad, and T. C. Petersen, arXiv:1611.05757 [hep-ph] [Search inSPIRE].
[22] G. C. Dorsch, S. J. Huber, T. Konstandin, and J. M. No, J. Cosmol. Astropart. Phys. **05**, 052 (2017).
[23] C.-Y. Chen, H.-L. Li, and M. Ramsey-Musolf, Phys. Rev. D **97**, 015020 (2018).
[24] S. Kanemura, M. Kubota, and K. Yagyu, J. High Energy Phys. **08**, 026 (2020).
[25] N. Blinov, J. Kozaczuk, D. E. Morrissey, and C. Tamarit, Phys. Rev. D **92**, 035012 (2015).
[26] A. Hammerschmitt, J. Kripfganz, and M.G. Schmidt, Z. Phys. C **64**, 105 (1994).
[27] L. Fromme, S. J. Huber, and M. Seniuch, J. High Energy Phys. **11**, 038 (2006).
[28] E. Witten, Phys. Rev. D **30**, 272 (1984).
[29] C. J. Hogan, Mon. Not. Roy. Astron. Soc. **218**, 629 (1986).
[30] C. Caprini et al., J. Cosmol. Astropart. Phys. **04**, 001 (2016).
[31] P. Amaro-Seoane et al., arXiv:1702.00786 [astro-ph.IM] [Search inSPIRE].
[32] C. Caprini et al., J. Cosmol. Astropart. Phys. **03**, 024 (2020).
[33] S. Profumo, M. J. Ramsey-Musolf, and G. Shaughnessy, J. High Energy Phys. **08**, 010 (2007).
[34] J. R. Espinosa, T. Konstandin, and F. Riva, Nucl. Phys. B **854**, 592 (2012).
[35] D. Curtin, P. Meade, and C.-T. Yu, J. High Energy Phys. **11**, 127 (2014).
[36] M. Jiang, L. Bian, W. Huang, and J. Shu, Phys. Rev. D **93**, 065032 (2016).
[37] F. P. Huang and C. S. Li, Phys. Rev. D **92**, 075014 (2015).
[38] G. Kurup and M. Perelstein, Phys. Rev. D **96**, 015036 (2017).
[39] Z. Kang, P. Ko, and T. Matsui, J. High Energy Phys. **02**, 115 (2018).
[40] T. Matsui, EPJ Web Conf. **168**, 05001 (2018).
[41] C.-W. Chiang, M. J. Ramsey-Musolf, and E. Senaha, Phys. Rev. D **97**, 015005 (2018).
[42] K. Hashino, M. Kakizaki, S. Kanemura, P. Ko, and T. Matsui, J. High Energy Phys. **06**, 088 (2018).
[43] F. P. Huang, Z. Qian, and M. Zhang, Phys. Rev. D **98**, 015014 (2018).
[44] C.-W. Chiang and B.-Q. Lu, J. High Energy Phys. **07**, 082 (2020).
[45] M. Carena, Z. Liu, and Y. Wang, J. High Energy Phys. **08**, 107 (2020).
[46] P. Ghorbani, arXiv:2010.15708 [hep-ph] [Search inSPIRE].
[47] L. Niemi, P. Schicho, and T. V. I. Tenkanen, arXiv:2103.07467 [hep-ph] [Search inSPIRE].
[48] D. Land and E. D. Carlson, Phys. Lett. B **292**, 107 (1992).
[49] A. Friedlander, I. Banta, J. M. Cline, and D. Tucker-Smith, Phys. Rev. D **103**, 055020 (2021).
[50] S. Fabian, F. Goertz, and Y. Jiang, arXiv:2012.12847 [hep-ph] [Search inSPIRE].
[51] X. Wang, F. P. Huang, and X. Zhang, Phys. Rev. D **101**, 015015 (2020).
[52] H. H. Patel and M. J. Ramsey-Musolf, Phys. Rev. D **88**, 035013 (2013).
[53] M. Chala, M. Ramos, and M. Spannowsky, Eur. Phys. J. C **79**, 156 (2019).
[54] N. F. Bell, M. J. Dolan, L. S. Friedrich, M. J. Ramsey-Musolf, and R. R. Volkas, J. High Energy Phys. **05**, 050 (2020).
[55] L. Niemi, M. Ramsey-Musolf, T. V. I. Tenkanen, and D. J. Weir, arXiv:2005.11332 [hep-ph] [Search inSPIRE].
[56] H. H. Patel, M. J. Ramsey-Musolf, and M. B. Wise, Phys. Rev. D **88**, 015003 (2013).
[57] S. Inoue, G. Ovanesyan, and M. J. Ramsey-Musolf, Phys. Rev. D **93**, 015013 (2016).
[58] F. P. Huang and X. Zhang, Phys. Lett. B **788**, 288 (2019).
[59] W. Chao, H.-K. Guo, and J. Shu, J. Cosmol. Astropart. Phys. **09**, 009 (2017).
[60] M. J. Ramsey-Musolf, P. Winslow, and G. White, Phys. Rev. D **97**, 123509 (2018).
[61] T. Vieu, A. P. Morais, and R. Pasechnik, J. Cosmol. Astropart. Phys. **07**, 014 (2018).
[62] A. P. Morais, R. Pasechnik, and T. Vieu, arXiv:1802.10109 [hep-ph] [Search inSPIRE].
[63] L. Bian and X. Liu, Phys. Rev. D **99**, 055003 (2019).
[64] R. Zhou, W. Cheng, X. Deng, L. Bian, and Y. Wu, J. High Energy Phys. **01**, 216 (2019).
[65] N. F. Bell, M. J. Dolan, L. S. Friedrich, M. J. Ramsey-Musolf, and R. R. Volkas, J. High Energy Phys. **19**, 012 (2020).
[66] A. P. Morais and R. Pasechnik, J. Cosmol. Astropart. Phys. **04**, 036 (2020).
[67] L. Bian, H.-K. Guo, Y. Wu, and R. Zhou, Phys. Rev. D **101**, 035011 (2020).
[68] S. Baum, M. Carena, N. R. Shah, C. E. M. Wagner, and Y. Wang, arXiv:2009.10743 [hep-ph] [Search inSPIRE].

[69] T. Ghosh, H.-K. Guo, T. Han, and H. Liu, arXiv:2012.09758 [hep-ph] [Search inSPIRE].
[70] T. Matsui, T. Nomura, and K. Yagyu, arXiv:2102.09247 [hep-ph] [Search inSPIRE].
[71] S. Kanemura, S. Kiyoura, Y. Okada, E. Senaha, and C. P. Yuan, Phys. Lett. B **558**, 157 (2003).
[72] S. Kanemura, Y. Okada, and E. Senaha, Phys. Lett. B **606**, 361 (2005).
[73] J. Braathen and S. Kanemura, Eur. Phys. J. C **80**, 227 (2020).
[74] F. Arco, S. Heinemeyer, and M. J. Herrero, Eur. Phys. J. C **80**, 884 (2020).
[75] M. Cepeda et al., CERN Yellow Rep. Monogr. **7**, 221 (2019).
[76] K. Fujii et al., arXiv:1506.05992 [hep-ex] [Search inSPIRE].
[77] V. Corbin and N. J. Cornish, Class. Quant. Grav. **23**, 2435 (2006).
[78] H. Kudoh, A. Taruya, T. Hiramatsu, and Y. Himemoto, Phys. Rev. D **73**, 064006 (2006).
[79] V. D. Barger, J. L. Hewett, and R. J. N. Phillips, Phys. Rev. D **41**, 3421 (1990).
[80] Y. Grossman, Nucl. Phys. B **426**, 355 (1994).
[81] M. Aoki, S. Kanemura, K. Tsumura, and K. Yagyu, Phys. Rev. D **80**, 015017 (2009).
[82] M. Quiros, Proc. ICTP Summer School in High-Energy Physics and Cosmology, p. 187 (1999) [arXiv:hep-ph/9901312] [Search inSPIRE].
[83] J. M. Cline, K. Kainulainen, and M. Trott, J. High Energy Phys. **11**, 089 (2011).
[84] L. Dolan and R. Jackiw, Phys. Rev. D **9**, 3320 (1974).
[85] E. J. Weinberg and A. Wu, Phys. Rev. D **36**, 2474 (1987).
[86] R. R. Parwani, Phys. Rev. D **45**, 4695 (1992); 48, 5965 (1993) [erratum].
[87] P. B. Arnold and O. Espinosa, Phys. Rev. D **47**, 3546 (1993); 50, 6662 (1994) [erratum].
[88] M. Laine, M. Meyer, and G. Nardini, Nucl. Phys. B **920**, 565 (2017).
[89] M. E. Carrington, Phys. Rev. D **45**, 2933 (1992).
[90] N. Blinov, S. Profumo, and T. Stefaniak, J. Cosmol. Astropart. Phys. **07**, 028 (2015).
[91] N. G. Deshpande and E. Ma, Phys. Rev. D **18**, 2574 (1978).
[92] M. Sher, Phys. Rept. **179**, 273 (1989).
[93] S. Nie and M. Sher, Phys. Lett. B **449**, 89 (1999).
[94] S. Kanemura, T. Kasai, and Y. Okada, Phys. Lett. B **471**, 182 (1999).
[95] S. Kanemura, T. Kubota, and E. Takasugi, Phys. Lett. B **313**, 155 (1993).
[96] A. G. Akeroyd, A. Arhrib, and E.-M. Naimi, Phys. Lett. B **490**, 119 (2000).
[97] A. Barroso, P. M. Ferreira, I. P. Ivanov, and R. Santos, J. High Energy Phys. **06**, 045 (2013).
[98] I. P. Ivanov and J. P. Silva, Phys. Rev. D **92**, 055017 (2015).
[99] C. L. Wainwright, Comput. Phys. Commun. **183**, 2006 (2012).
[100] H. E. Haber and D. O'Neil, Phys. Rev. D **83**, 055017 (2011).
[101] J. Haller, A. Hoecker, R. Kogler, K. Mönig, T. Peiffer, and J. Stelzer, Eur. Phys. J. C **78**, 675 (2018).
[102] A. Arhrib, R. Benbrik, H. Harouiz, S. Moretti, and A. Rouchad, arXiv:1810.09106 [hep-ph] [Search inSPIRE].
[103] G. Aad et al., Phys. Rev. D **101**, 012002 (2020).
[104] V. Khachatryan et al., Phys. Lett. B **759**, 369 (2016).
[105] M. Aaboud et al., Phys. Lett. B **783**, 392 (2018).
[106] A. M. Sirunyan et al., J. High Energy Phys. **03**, 055 (2020).
[107] F. Kling, S. Su, and W. Su, J. High Energy Phys. **06**, 163 (2020).
[108] S. Semlali, H. Day-Hall, S. Moretti, and R. Benbrik, Phys. Lett. B **810**, 135819 (2020).
[109] ATLAS Collaboration, Tech. Rep. ATLAS-CONF-2019-049, CERN, Geneva. (2019),http://cds.cern.ch/record/2667570.
[110] A. Kosowsky, M. S. Turner, and R. Watkins, Phys. Rev. D **45**, 4514 (1992).
[111] A. Kosowsky, M. S. Turner, and R. Watkins, Phys. Rev. Lett. **69**, 2026 (1992).
[112] A. Kosowsky and M. S. Turner, Phys. Rev. D **47**, 4372 (1993).
[113] M. Kamionkowski, A. Kosowsky, and M. S. Turner, Phys. Rev. D **49**, 2837 (1994).
[114] C. Caprini, R. Durrer, and G. Servant, Phys. Rev. D **77**, 124015 (2008).
[115] S. J. Huber and T. Konstandin, J. Cosmol. Astropart. Phys. **09**, 022 (2008).
[116] M. Hindmarsh, S. J. Huber, K. Rummukainen, and D. J. Weir, Phys. Rev. Lett. **112**, 041301 (2014).
[117] J. T. Giblin Jr and J. B. Mertens, J. High Energy Phys. **12**, 042 (2013).
[118] J. T. Giblin and J. B. Mertens, Phys. Rev. D **90**, 023532 (2014).
[119] M. Hindmarsh, S. J. Huber, K. Rummukainen, and D. J. Weir, Phys. Rev. D **92**, 123009 (2015).

[120] C. Caprini and R. Durrer, Phys. Rev. D **74**, 063521 (2006).
[121] T. Kahniashvili, A. Kosowsky, G. Gogoberidze, and Y. Maravin, Phys. Rev. D **78**, 043003 (2008).
[122] T. Kahniashvili, L. Campanelli, G. Gogoberidze, Y. Maravin, and B. Ratra, Phys. Rev. D **78**, 123006 (2008); 79, 109901 (2009) [erratum].
[123] T. Kahniashvili, L. Kisslinger, and T. Stevens, Phys. Rev. D **81**, 023004 (2010).
[124] C. Caprini, R. Durrer, and G. Servant, J. Cosmol. Astropart. Phys. **12**, 024 (2009).
[125] P. Binetruy, A. Bohe, C. Caprini, and J.-F. Dufaux, J. Cosmol. Astropart. Phys. **06**, 027 (2012).
[126] J. R. Espinosa, T. Konstandin, J. M. No, and G. Servant, J. Cosmol. Astropart. Phys. **06**, 028 (2010).
[127] N. Seto, S. Kawamura, and T. Nakamura, Phys. Rev. Lett. **87**, 221103 (2001).
[128] S. Kawamura et al., Class. Quant. Grav. **28**, 094011 (2011).
[129] W.-R. Huand and Y.-L. Wu, Natl. Sci. Rev. **4**, 685 (2017).
[130] W.-H. Ruan, Z.-K. Guo, R.-G. Cai, and Y.-Z. Zhang, Int. J. Mod. Phys. A **35**, 2050075 (2020).
[131] J. Luo et al., Class. Quant. Grav. **33**, 035010 (2016).
[132] X.-C. Hu, X.-H. Li, Y. Wang, W.-F. Feng, M.-Y. Zhou, Y.-M. Hu, S.-C. Hu, J.-W. Mei, and C.-G. Shao, Class. Quant. Grav. **35**, 095008 (2018).
[133] H.-K. Guo, K. Sinha, D. Vagie, and G. White, J. Cosmol. Astropart. Phys. **01**, 001 (2021).
[134] D. Cutting, M. Hindmarsh, and D. J. Weir, Phys. Rev. Lett. **125**, 021302 (2020).
[135] X. Wang, F. P. Huang, and X. Zhang, J. Cosmol. Astropart. Phys. **05**, 045 (2020).
[136] D. Croon, O. Gould, P. Schicho, T. V. I. Tenkanen, and G. White, J. High Energy Phys. **04**, 055 (2021).
[137] H.-K. Guo, K. Sinha, D. Vagie, and G. White, arXiv:2103.06933 [hep-ph] [Search inSPIRE].
[138] O. Gould and T. V. I. Tenkanen, J. High Energy Phys. **06**, 069 (2021).
[139] F. Giese, T. Konstandin, and J. Van De Vis, J. Cosmol. Astropart. Phys. **07**, 057 (2020).
[140] S. Höche, J. Kozaczuk, A. J. Long, J. Turner, and Y. Wang, J. Cosmol. Astropart. Phys. **03**, 009 (2021).
[141] F. Giese, T. Konstandin, K. Schmitz, and J. Van De Vis, J. Cosmol. Astropart. Phys. **01**, 072 (2021).
[142] X. Wang, F. P. Huang, and X. Zhang, Phys. Rev. D **103**, 103520 (2021).
[143] X. Wang, F. P. Huang, and X. Zhang, arXiv:2011.12903 [hep-ph] [Search inSPIRE].
[144] C. Delaunay, C. Grojean, and J. D. Wells, J. High Energy Phys. **04**, 029 (2008).